Probing the Geometric and Electronic Structures of the Low-Temperature Azide Adduct and the Product-Inhibited Form of Oxidized Manganese Superoxide Dismutase†

Timothy A. Jackson,‡ Anush Karapetian,§ Anne-Frances Miller,§ and Thomas C. Brunold*,‡

Department of Chemistry, University of Wisconsin—Madison, Madison, Wisconsin 53706, and Department of Chemistry, University of Kentucky, Lexington, Kentucky 40506

Received June 29, 2004; Revised Manuscript Received October 27, 2004

ABSTRACT: The geometric and electronic structures of the six-coordinate azide adduct of oxidized manganese superoxide dismutase (Mn^{3+}SOD) that is formed at low temperatures, LT N_3−Mn^{3+}SOD, has been examined in detail through a combined spectroscopic/computational approach. Electronic absorption, circular dichroism (CD), magnetic CD (MCD) and variable-temperature, variable-field (VTVH) MCD spectroscopies were used to determine electronic transition energies and to obtain an estimate of zero-field splitting parameters for LT N_3−Mn^{3+}SOD. These experimental data were utilized in conjunction with semiempirical intermediate neglect of differential overlap/spectroscopic parametrization−configuration interaction (INDO/S−CI) and time-dependent density functional theory (TD-DFT) computations to evaluate hypothetical active-site models of LT N_3−Mn^{3+}SOD generated by constrained DFT geometry optimizations. Collectively, our spectroscopic/computational results indicate that N_3^- binding to Mn^{3+}SOD at low temperatures promotes neither protonation of the axial solvent ligand nor reorientation of the redox-active molecular orbital, both of which had been previously suggested. Using the same experimentally validated computational approach, models of the product-inhibited form of MnSOD were also developed and evaluated by their relative energies and TD-DFT-computed absorption spectra. On the basis of our computational results as well as previously published kinetic data, we propose that the product-inhibited form of MnSOD is best described as a side-on peroxo-Mn^{3+} adduct possessing an axial H_2O ligand. Notably, attempts to generate a stable hydroperoxo-Mn^{3+}SOD species by protonation of the proximal O atom of the hydroperoxo ligand resulted in dissociation of HOO^- and eventual H^+ transfer from Tyr34 to HOO^-, generating deprotonated Tyr34 and H_2O_2. The implications of these results with respect to the mechanism of $O_2^{\cdot -}$ dismutation by MnSOD are discussed.

Mn-dependent superoxide dismutases (MnSODs)[1] are enzymes found in both bacteria and higher organisms (including humans), where they catalyze the disproportionation of the harmful superoxide radical anion ($O_2^{\cdot -}$) that is produced in small quantities by processes such as respiration and photosynthesis (*1*−*3*). These enzymes are typically isolated as dimers or tetramers containing one Mn ion per subunit. X-ray crystallographic studies of MnSODs (*4*−*6*) have revealed that the active-site Mn ion is ligated by four amino acid residues and one solvent molecule in a trigonal bipyramid, where, using the numbering scheme of *Escherichia coli* MnSOD, His171, His81, and Asp167 form the equatorial plane, while His26 and a solvent molecule occupy the axial positions (top of Figure 1). Both experimental and theoretical studies have shown that the axially ligated solvent molecule is OH^- in the oxidized Mn^{3+}SOD state but acquires a proton to become H_2O upon reduction of the metal ion to yield Mn^{2+}SOD (eq 1) (*7*, *8*). The kinetics of superoxide

$$Mn^{3+}SOD^{OH} + e^- + H^+ \rightarrow Mn^{2+}SOD^{H_2O} \qquad (1)$$

dismutation by MnSODs isolated from a variety of organisms (including *E. coli* and humans) have been studied in detail by a number of research groups (*9*−*13*). These studies showed that this reaction proceeds by a two-step, ping-pong mechanism in which both steps are first-order in $O_2^{\cdot -}$ (eq

† This work was supported by the University of Wisconsin, National Institute of Health Grant GM 64631 (to T.C.B.), University of Wisconsin Biophysics Training Grant (to T.A.J.), National Science Foundation Grant MCB0129599, and Kentucky Science and Engineering Foundation Grant 172-RDE-002 (to A.-F.M.).

* To whom correspondence should be addressed: 1101 University Ave., Madison, WI 53706. Telephone: (608) 265-9056. Fax: (608) 262-6143. E-mail: brunold@chem.wisc.edu.

‡ University of Wisconsin—Madison.

§ University of Kentucky.

[1] Abbreviations: ADF, Amsterdam Density Functional; CD, circular dichroism; CT, charge transfer; DFT, Density Functional Theory; DOMO, doubly occupied molecular orbital; EDTA, ethylenediaminetetraacetic acid; EPR, electron paramagnetic resonance; INDO/S−CI, intermediate neglect of differential overlap/spectroscopic parametrization−configuration interaction; LF, ligand field; LMCT, ligand-to-metal charge transfer; LT, low temperature; LUMO, lowest-unoccupied molecular orbital; MCD, magnetic circular dichroism; MO, molecular orbital; NIR, near infrared; PDB, Protein Data Bank; RT, room temperature; SOD, superoxide dismutase; SOMO, singly occupied molecular orbital; TD, time dependent; UV, ultraviolet; VTVH, variable temperature, variable field; WT, wild type; ZFS, zero-field splitting.

10.1021/bi048639t CCC: $30.25
Published on Web 01/12/2005

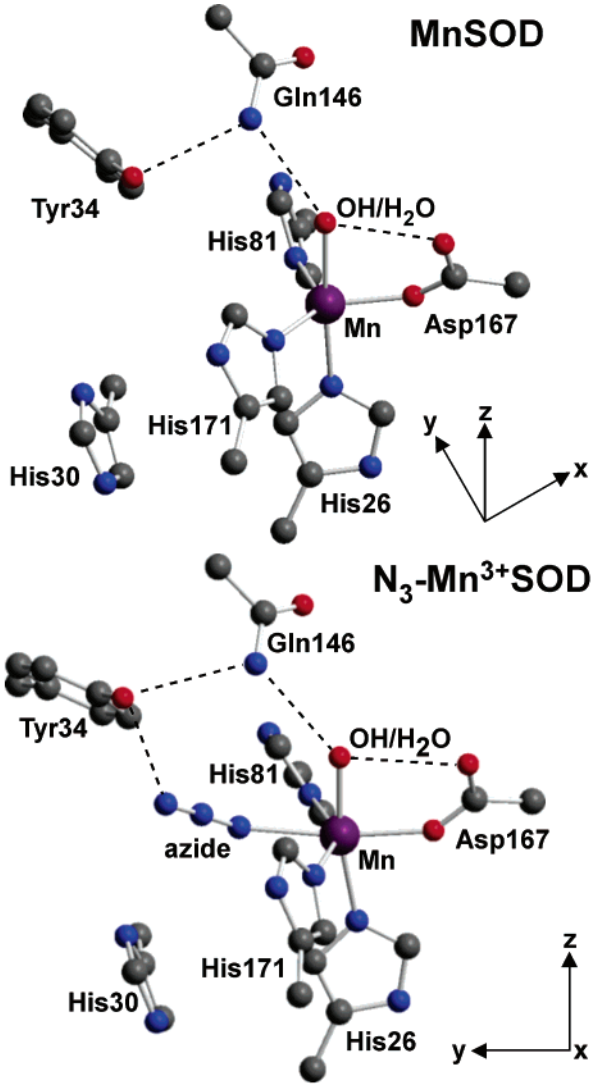

FIGURE 1: Active-site structures of *E. coli* MnSOD (top) and *T. thermophilus* N_3−Mn^{3+}SOD (bottom) based on coordinates from the PDB files 1VEW and 1MNG-L, respectively. Dashed lines indicate important H-bonding interactions. Note that for both structures the *E. coli* amino acid numbering scheme is used. The axis systems are aligned according to the **D**-tensor orientations obtained from INDO/S−CI computations on our Mn^{3+}SOD and N_3−$Mn^{3+}SOD^{OH}$ models.

2). At high $O_2^{\cdot-}$ concentrations, the catalytic cycle is compli-

$$Mn^{3+}SOD^{OH} + O_2^{\cdot-} + H^+ \rightarrow Mn^{2+}SOD^{H_2O} + O_2 \quad (2a)$$

$$Mn^{2+}SOD^{H_2O} + O_2^{\cdot-} + H^+ \rightarrow Mn^{3+}SOD^{OH} + H_2O_2 \quad (2b)$$

cated by the formation of an inhibited form of the enzyme that is, however, able to convert back to an active form (Scheme 1). Recently, it has been suggested that formation of this inhibited form of the enzyme may be biologically significant, because human embryonic kidney cells expressing a MnSOD mutant that shows decreased product inhibition were less prolific and tumorigenic, presumably because of enhanced H_2O_2 production (*14*).

While little is known about the geometric structure of the product-inhibited form of MnSOD (hereafter referred to as the dead-end complex), it has been noted that the absorption spectrum of this species resembles that of the low-temper-

Scheme 1

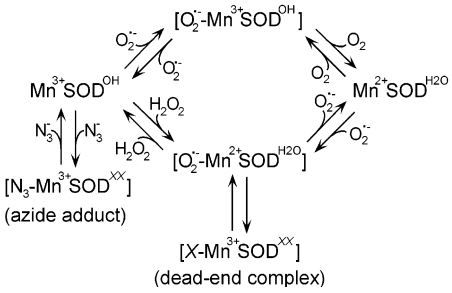

ature azide adduct of Mn^{3+}SOD (termed LT N_3−Mn^{3+}SOD) (*15*). It has been proposed that the dead-end complex results from the oxidative addition of $O_2^{\cdot-}$ to Mn^{2+}SOD to yield a side-on peroxo-Mn^{3+} adduct (*12*). The existence of this structural motif in a synthetic Mn^{3+} complex (*16*) lends support to this proposal. However, the absorption spectrum of the synthetically generated side-on peroxo-Mn^{3+} adduct differs considerably from that reported for the dead-end complex of MnSOD; i.e., $\lambda_{max} \approx 580-560$ nm ($\epsilon \approx 70$ M^{-1} cm^{-1}) for the synthetic complex (*16*), versus $\lambda_{max} \approx 410$ and 650 nm ($\epsilon \approx 700$ and 230 M^{-1} cm^{-1}, respectively) for the dead-end complex (*12*, *13*). Moreover, formation of a side-on peroxo-Mn^{3+} core for MnSOD would probably require ligand dissociation, because a side-on-bound peroxo ligand tends to occupy two coordination sites (*16*, *17*).

While earlier studies of room-temperature (RT) N_3−Mn^{3+}-SOD had suggested that either coordinated solvent or Asp167 is indeed capable of dissociating at physiological temperatures upon small anion binding to the Mn^{3+} center (*15*, *18*, *19*), we have recently shown that dissociation of either of these ligands is unlikely and that the temperature-dependent active-site conversion of N_3−Mn^{3+}SOD actually involves azide dissociation at higher temperatures (*20*). While a direct spectroscopic study of the dead-end complex is complicated by its rapid decay (*12*, *21*), insight into the nature of this structurally ill-defined species could potentially be obtained through a detailed analysis of the geometric and electronic structures of the spectroscopically similar LT N_3−Mn^{3+}SOD species.

Whittaker and Whittaker performed the first detailed study of N_3−Mn^{3+}SOD using a combination of RT absorption and circular dichroism (CD) spectroscopies along with LT magnetic CD (MCD) and variable-temperature, variable-field (VTVH) MCD spectroscopies (*22*). Because RT absorption and CD spectra suggested that the addition of N_3^- to Mn^{3+}-SOD does not result in an expansion of the coordination sphere, LT and VTVH MCD data were interpreted within the context of a five-coordinate Mn^{3+} center. Specifically, on the basis of the drastic alterations of MCD and VTVH MCD data of Mn^{3+}SOD upon the addition of N_3^-, it was suggested that the presence of this anion results in a change from a $3d_{z^2}$ to a $3d_{x^2-y^2}$ ground state (using the widely adopted hole formalism) and, consequently, from a trigonal bipyramidal (resting Mn^{3+}SOD) to square pyramidal (N_3−Mn^{3+}-SOD) coordination geometry (*22*). However, more recent variable-temperature studies of N_3−Mn^{3+}SOD revealed that, while the active-site Mn^{3+} ion of this species is indeed five-coordinate at RT, N_3−Mn^{3+}SOD is thermochromic (T_m = 205 K for *E. coli* N_3−Mn^{3+}SOD) (*15*) and converts to a pseudo-octahedral, six-coordinate N_3−Mn^{3+} adduct at LT

that has been characterized by X-ray crystallography (*5*). Thus, on the basis of these later findings, it follows that differences in the MCD spectra of resting Mn^{3+}SOD and LT N_3-Mn^{3+}SOD are actually due to a change in coordination number rather than a structural conversion within a five-coordination geometry. Furthermore, the proposal that LT N_3-Mn^{3+}SOD possesses a $3d_{x^2-y^2}$ ground state appears questionable, because (i) a Mn^{3+} ion in a pseudo-octahedral geometry may adopt either a $3d_{z^2}$ or a $3d_{x^2-y^2}$ ground state and (ii) the interpretation of VTVH MCD data obtained for LT N_3-Mn^{3+}SOD, which led to the original ground-state assignment (*22*), was performed before a quantitative analysis of such data in terms of ground-state spin Hamiltonian parameters and transition polarizations had been developed. Additionally, while electron paramagnetic resonance (EPR) studies were able to corroborate the orbital ground-state assignment for Mn^{3+}SOD, LT N_3-Mn^{3+}SOD is EPR-silent at X-band frequency in parallel mode (*23*). Because knowledge of the orbital ground state of LT N_3-Mn^{3+}SOD has important implications for the orientation of the Mn 3d-based redox-active molecular orbital in substrate$-Mn^{3+}$SOD adducts that may be transiently formed during the catalytic cycle, reinvestigation of spectroscopic data obtained for LT N_3-Mn^{3+}SOD appears warranted.

In this study, we have used absorption, CD, MCD, and VTVH MCD spectroscopies in combination with intermediate neglect of differential overlap/spectroscopic parametrization−configuration interaction (INDO/S−CI), Density Functional Theory (DFT), and time-dependent DFT (TD-DFT) computations to generate an experimentally validated electronic structure description of LT N_3-Mn^{3+}SOD. Our quantitative analysis of VTVH MCD data obtained for LT N_3-Mn^{3+}SOD concurs with INDO/S−CI computations on an active-site model of this species, both yielding zero-field splitting (ZFS) parameters that are consistent with a $3d_{z^2}$ ground state, in contrast to a previous proposal (*22*). Given the success of our computational methods in reproducing the essential structural and electronic features of LT N_3-Mn^{3+}SOD, hypothetical active-site models of the dead-end complex could be generated using DFT geometry optimization and evaluated based on their TD-DFT-computed absorption spectra. Our results indicate that the absorption spectrum of the dead-end complex is consistent with both a side-on peroxo-Mn^{3+} complex or an end-on hydroperoxo-Mn^{3+} complex, the latter resulting from H^+ transfer from coordinated water to the terminal O atom of the nascent peroxo ligand. To discriminate between these two possible descriptions of the dead-end complex, experimental data reported in the literature are carefully evaluated and a molecular mechanism for the reduction of superoxide by Mn^{2+}SOD is proposed.

MATERIALS AND METHODS

Sample Preparation. Wild-type (WT) MnSOD was purified from *E. coli* according to an improved version (Karapetian, A. and Miller, A.-F., unpublished results) of the standard procedure (*24*, *25*). The Mn^{3+}SOD species used in this study were ∼2−3 mM in 50 mM phosphate buffer (pH 7.0). N_3-Mn^{3+}SOD was generated by incubating a 2.05 mM solution of Mn^{3+}SOD with 183 mM NaN_3 in 50 mM phosphate buffer (pH 7.0) or, to create a low pH sample, by treating 2.38 mM Mn^{3+}SOD with 262 mM NaN_3 in 50 mM 2-morpholinoethanesulfonic acid (MES) buffer (pH 5.5). The specific conditions used for all samples are given in the captions of Figures 2 and 3.

Absorption, CD, and MCD Spectroscopies. LT absorption, CD, and MCD spectra were collected on a spectropolarimeter (Jasco J-715) in conjunction with a magnetocryostat (Oxford Instruments SM-4000) capable of fields up to 8 T. To ensure glass formation upon freezing, LT samples were prepared in 55% (v/v) glycerol and 50 mM phosphate buffer (pH 7.0). Because glycerol could potentially perturb the active site, RT absorption and CD data of N_3-Mn^{3+}SOD were measured both in the absence and presence of glycerol. The close resemblance of these data sets indicates that glycerol has no effect on the active-site properties of N_3-Mn^{3+}SOD.

The LT MCD spectrum of N_3-Mn^{3+}SOD presented in this study was corrected for the presence of a small fraction of resting enzyme by subtraction of a properly scaled MCD spectrum of Mn^{3+}SOD (∼9%). This correction eliminated a negative MCD feature from the raw data at ∼16 500 cm^{-1}. On the basis of its VTVH MCD saturation behavior, this band was solely due to resting Mn^{3+}SOD and not LT N_3-Mn^{3+}SOD (Figure S1 in the Supporting Information). VTVH MCD data were analyzed using a fitting program developed by Dr. Frank Neese (MPI Mülheim, Germany) (*26*).

Computations: (A) Active-Site Models. The active-site models for LT N_3-Mn^{3+}SOD, O_2-Mn^{3+}SOD, HOO$-Mn^{3+}$SOD, H30V O_2-Mn^{3+}SOD, and H30V HOO$-Mn^{3+}$SOD were derived from the X-ray structure coordinates of N_3-Mn^{3+}SOD from *Thermus thermophilus* (PDB file 1MNGL) (*5*) or, for the last two models, of the H30V mutant of the human enzyme (PDB file 1N0N) (*27*). The first-sphere Asp and His ligands were modeled by acetate and 4-methylimidazole, respectively, and the second-sphere Gln and Tyr residues were represented by acetamide and 4-methylphenol, respectively. For H30V O_2-Mn^{3+}SOD and H30V HOO$-Mn^{3+}$SOD, Val30 was modeled by 2-methylpropane. Models with a side-on peroxo ligand with either OH^- or H_2O as the axial solvent ligand, termed (η^2-O_2)$-Mn^{3+}SOD^{OH}$ and (η^2-O_2)$-Mn^{3+}SOD^{H_2O}$, respectively, were generated by replacing N_3^- with O_2^{2-}, where the initial geometry of the O_2^{2-} ligand with respect to the Mn^{3+} ion was based on X-ray structure data of synthetic side-on peroxo-Mn^{3+} complexes (*16*). Specifically, Mn−O(peroxo) bond lengths of 1.85 Å and an O−O bond length of 1.43 Å were used, yielding an O−Mn−O angle of 45°. The O_2^{2-} ligand was oriented such that the Mn−O(Asp167) bond axis roughly bisected the O−O bond. Models with an end-on hydroperoxo ligand were generated by replacing N_3^- with HOO^- and using initial O−Mn and O−O distances of 1.94 and 1.48 Å, respectively, along with a Mn−O−O angle of 148°. A H^+ was added at the terminal and proximal O(peroxo) atoms to generate HOO$-Mn^{3+}$SOD and O(H)O$-Mn^{3+}$SOD, respectively. For these models, the coordinated solvent was assumed to be OH^- because (i) generation of a hydroperoxo ligand would presumably involve proton transfer from coordinated H_2O to the nascent peroxo ligand and (ii) N_3-Mn^{3+}SOD, which is electronically similar to HOO$-Mn^{3+}$SOD, coordinates OH^- rather than H_2O (*vide infra*).

(B) DFT Geometry Optimizations. Various computational approaches have been applied in the past to obtain reasonable structures for the active site of Mn^{3+}SOD in the resting state as well as for the corresponding azide and superoxide adducts

(*7*, *28*−*31*). One significant difference among these approaches relates to constraints placed on the Mn^{3+}SOD active site during the energy minimization. While, in some cases, the coordinates of all atoms were allowed to vary during energy minimization (*28*, *31*), in others, certain atomic coordinates or internal degrees of freedom were fixed (*7*, *29*, *30*). The disadvantage of an energy minimization with respect to all atomic coordinates when using a truncated active-site model is that constraints imposed on the active site by the protein backbone are neglected and steric and/or H-bonding interactions between second- and first-sphere residues cannot be incorporated unless second-sphere residues are explicitly included in the model.[2] However, in geometry optimizations of structurally ill-defined species, such as peroxo- or hydroperoxo-Mn^{3+}SOD species, the active-site model must be allowed a certain degree of conformational flexibility during the energy minimization procedure to obtain a realistic structure. Thus, to allow for some degree of conformational flexibility during our DFT energy minimizations, while accounting for some of the geometric constraints imposed on the active site by the protein matrix, the coordinates of the terminal methyl groups of the first-sphere amino acid residues, which model the H_3C_β groups (because all first-sphere residues were truncated at the C_β positions), were held fixed in all of the DFT energy minimizations described in this study. Furthermore, second-sphere residues, which, on the basis of X-ray structure data, (*5*) interact with coordinated substrate analogues or coordinated solvent (i.e., Gln146 and Tyr34), were explicitly included.

The Amsterdam Density Functional (ADF) 2003.01 software package (*32*−*34*) was used to carry out DFT energy minimizations. These computations were performed on a cluster consisting of Intel Xeon processors (Ace Computers) using a basis set consisting of uncontracted triple-ζ Slater-type orbitals including a single set of polarization functions (ADF basis set IV), an integration constant of 3.0, and the local density approximation of Vosko, Wilk, and Nusair (*35*) with the nonlocal gradient corrections of Becke (*36*) and Perdew (*37*). Core orbitals were frozen through 1s (O, N, and C) and 2p (Mn). Calculations were converged to the $S = 2$ and $S = {}^5/_2$ spin states for Mn^{3+} and Mn^{2+} species, respectively. The coordinates of all DFT energy-minimized models presented in this study are included in Tables S1−S11 in the Supporting Information.

(C) Calculation of Ground- and Excited-State Properties. The ORCA 2.2 software package, developed by Dr. Frank Neese (*38*), was used to perform semiempirical INDO/S−CI, single-point DFT, and TD-DFT calculations on the geometry-optimized active-site models. For INDO/S−CI computations, the ORCA program employs the model of Zerner and co-workers (*39*, *40*), the valence-shell ionization potentials and Slater−Condon parameters listed by Bacon and Zerner (*41*), the standard interaction factors $f_{p\sigma p\sigma} = 1.266$ and $f_{p\pi p\pi} = 0.585$, and the following spin−orbit coupling constants: $\zeta_{3d}(Mn) = 300\ cm^{-1}$, $\zeta_{4p}(Mn) = 334\ cm^{-1}$, $\zeta_{2p}(N) = 76\ cm^{-1}$, and $\zeta_{2p}(O) = 150\ cm^{-1}$. Restricted open-shell Hartree−Fock self-consistent field calculations for Mn^{3+}-containing active-site models were tightly converged on the quintet ground state. Configuration interaction (CI) with single- and double-electron excitations (CISD) was then included within the $S = 2$ spin-state manifold, and CI with single-electron excitations (CIS) was included within the $S = 1$ spin-state manifold. For $N_3-Mn^{3+}SOD^{OH}$, the CISD active space for the quintet states included single excitations within the 50 highest energy doubly occupied molecular orbitals (DOMOs), the 4 singly occupied MOs (SOMOs), and the 68 lowest energy virtual MOs, as well as double excitations within the 31 highest energy DOMOs, the 4 SOMOs, and the 4 lowest energy virtual MOs. For $N_3-Mn^{3+}SOD^{H_2O}$, the CISD active space for the quintet states consisted of single excitations within the 46 highest energy DOMOs, the 4 SOMOs, and the 52 lowest energy virtual MOs, as well as double excitations within the 32 highest energy DOMOs, the 4 SOMOs, and the 5 lowest energy virtual MOs. For both models, the CIS active space of the triplet states included single-electron excitations within the 4 SOMOs and the lowest unoccupied molecular orbital (LUMO). The completeness of these active spaces was monitored by the insensitivity of the calculated ZFS parameters to the inclusion of additional one- and two-electron excitations.

Single-point DFT calculations using the ORCA program employed Becke's three-parameter hybrid functional for exchange (*42*, *43*) combined with the Lee−Yang−Parr correlation functional (*44*) (B3LYP/G) and the default 20% Hartree−Fock exchange. The SV(P) (Ahlrichs polarized split valence) basis (*45*) with the SV/C auxiliary basis (*46*) was used for all atoms except Mn, where the TZVP (Ahlrichs polarized triple-ζ valence) basis (*47*) in conjunction with the TZV/J auxiliary basis was used. The size of the integration grid used for all calculations was 3 (Lebedev 194 points). Isosurface plots of MOs were generated with the gOpenMol program developed by Laaksonen (*48*, *49*) using the isodensity values of $0.03\ b^{-3}$.

Electronic excitation energies and absorption intensities for all Mn^{3+} active-site models included in this study were determined by the TD-DFT (*50*−*52*) method within the Tamm−Dancoff approximation (*53*, *54*), employing the same functionals, basis sets, and integration grid as described above for the single-point DFT computations. The resolution of the identity approximation in calculating the Coulomb term (*55*) was used to ensure convergence of all TD-DFT calculations. In each case, 40 excited states were calculated by including all one-electron excitations within an energy window of ±3 Hartrees ($\pm 658\ 000\ cm^{-1}$) with respect to the HOMO/LUMO energies.

(D) ΔpK Calculations. The change in p*K* (Δp*K*) of the axial solvent ligand of LT N_3-Mn^{3+}SOD relative to resting Mn^{2+}SOD was calculated according to a previously developed methodology (*30*, *56*) based on the work of Noodleman and co-workers (*7*, *57*, *58*). A Δp*K* rather than an absolute p*K* value was computed because the calculation of the latter would require predicting changes in solvation energies and zero-point energies between deprotonated and protonated states, which is more challenging computationally (*59*). The calculation of a Δp*K* allows us to ignore these contributions, provided that changes in solvation energies and zero-point energies are similar between the species of interest, as is expected to be the case for the equally charged N_3-Mn^{3+}-

[2] In this study, attempts to perform DFT geometry optimizations of N_3-Mn^{3+}SOD with respect to all atomic coordinates led to unrealistically long Mn−N(His) bond lengths of >2.4 Å.

SOD and Mn^{2+}SOD active sites. While it would also be desirable to calculate a ΔpK between N_3-Mn^{3+}SOD and resting Mn^{3+}SOD to explore how the coordination of azide to Mn^{3+} affects the acidity of the axial solvent ligand, these active sites differ in overall charge; thus, differences in solvation energies between the protonated and deprotonated states of N_3-Mn^{3+}SOD and Mn^{3+}SOD may differ substantially.

To obtain a ΔpK, constrained DFT energy minimizations were first performed for models of N_3-Mn^{3+}SOD with both axial hydroxide ($N_3-Mn^{3+}SOD^{OH}$) and water ($N_3-Mn^{3+}SOD^{H_2O}$) ligands, where the coordinates of the H_3C_β groups and second-sphere atoms not involved in the H-bond network were held fixed. The energies of these species at convergence were then used to calculate the gas-phase deprotonation energy of the axial water ligand of N_3-Mn^{3+}SOD, $\epsilon_{deprot}[N_3-Mn^{3+}SOD]$, according to eq 3a. Models for resting Mn^{2+}SOD were generated based on our previous studies of this system (*30*), where the X-ray structure of redox heterogeneous MnSOD (1VEW) (*6*) was used as a starting point for a constrained DFT energy minimization using the same constraints as for our $N_3-Mn^{3+}SOD^{OH}$ and $N_3-Mn^{3+}SOD^{H_2O}$ models. The corresponding gas-phase deprotonation energy for resting Mn^{2+}SOD, $\epsilon_{deprot}[Mn^{2+}SOD]$, was then calculated according to eq 3b. The gas-phase deprotonation

$$\epsilon_{deprot}[N_3-Mn^{3+}SOD] = \epsilon[N_3-Mn^{3+}SOD^{OH}] + \epsilon[H^+] - \epsilon[N_3-Mn^{3+}SOD^{H_2O}] \quad (3a)$$

$$\epsilon_{deprot}[Mn^{2+}SOD] = \epsilon[Mn^{2+}SOD^{OH}] + \epsilon[H^+] - \epsilon[Mn^{2+}SOD^{H_2O}] \quad (3b)$$

energies calculated by eq 3 were subsequently used to determine the difference in gas-phase proton affinity, $\Delta PA_{(g)}$, in kcal/mol between N_3-Mn^{3+}SOD and Mn^{2+}SOD according to eq 4. Note that in evaluating $\Delta PA_{(g)}$ the $\epsilon[H^+]$ terms present in eq 3 cancel and therefore do not need to be determined. Finally, $\Delta PA_{(g)}$ was converted to a ΔpK using the standard conversion factor relating kcal/mol to pH units (eq 5), where $RT = 0.59$ kcal/mol at $T = 298$ K.

$$\Delta PA_{(g)} = \epsilon_{deprot}[N_3-Mn^{3+}SOD] - \epsilon_{deprot}[Mn^{2+}SOD] \quad (4)$$

$$\Delta pK = \{\Delta PA_{(g)}\}/2.3RT \quad (5)$$

RESULTS AND ANALYSIS

Spectroscopy. (A) Effects of N_3^- on the MCD Spectrum of Mn^{3+}SOD at LT. As shown in Figure 2, the LT MCD spectrum of Mn^{3+}SOD is greatly perturbed by the addition of N_3^- to the enzyme. While in each spectrum a prominent, positive feature is observed at ~21 500 cm^{-1}, the spectrum of Mn^{3+}SOD exhibits an intense, negative feature at ~17 000 cm^{-1} that has no counterpart in the LT N_3-Mn^{3+}SOD spectrum. Furthermore, the addition of N_3^- to Mn^{3+}SOD causes a loss of MCD intensity across the entire visible spectral region. Because this region is dominated by the four spin-allowed d → d (ligand field, LF) transitions of the $3d^4$ Mn^{3+} ion (*20*, *22*), the striking changes caused by N_3^- addition reflect a major perturbation of the LF excited-state

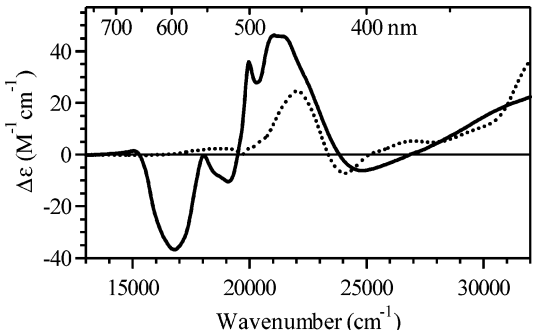

FIGURE 2: MCD spectra (4.5 K, 7 T) of Mn^{3+}SOD (—) and N_3-Mn^{3+}SOD (•••). Conditions, 3 mM Mn^{3+}SOD in 50 mM phosphate buffer (pH 7.0) and 50% (v/v) glycerol for Mn^{3+}SOD and 2.05 mM Mn^{3+}SOD and 183 mM NaN_3 in 50 mM phosphate buffer (pH 7.0) and 55% (v/v) glycerol for N_3-Mn^{3+}SOD.

energies, implying drastically different coordination geometries for Mn^{3+}SOD and LT N_3-Mn^{3+}SOD. Because a previous, qualitative analysis of VTVH MCD data for these species suggested that Mn^{3+}SOD and LT N_3-Mn^{3+}SOD possess different orbital ground states (i.e., $3d_{z^2}$ and $3d_{x^2-y^2}$, respectively), the differences in the MCD spectra of these two systems were originally attributed to a conversion from a trigonal bipyramidal (resting Mn^{3+}SOD) to a square pyramidal (LT N_3-Mn^{3+}SOD) geometry with retention of a five-coordinate Mn^{3+} ion (*22*). However, subsequent studies revealed that N_3^- binds to Mn^{3+}SOD at LT to increase the coordination number from 5 to 6 (*5*, *15*, *18*). Thus, differences in the MCD spectra of Mn^{3+}SOD and LT N_3-Mn^{3+}SOD reflect this conversion of the trigonal bipyramidal resting active site to a six-coordinate N_3-Mn^{3+} adduct with distorted octahedral geometry. In light of this more recent information regarding the Mn^{3+} coordination environment, the conclusion that LT N_3-Mn^{3+}SOD possesses a $3d_{x^2-y^2}$ ground state also appears questionable. Therefore, we have reinvestigated the spectroscopic properties of LT N_3-Mn^{3+}SOD to address this issue.

(B) LT N_3-Mn^{3+}SOD Absorption, CD, and MCD Spectra. The LT absorption spectrum of N_3-Mn^{3+}SOD (top of Figure 3) exhibits a weak feature at ~18 000 cm^{-1} ($\epsilon \approx 100$ M^{-1} cm^{-1}), a broad envelope centered at ~23 000 cm^{-1} ($\epsilon \approx 400$ M^{-1} cm^{-1}), and the onset of intense features at higher energies (>30 000 cm^{-1}, $\epsilon >700$ M^{-1} cm^{-1}). The absorption intensities of the bands in the visible region are much lower than those observed for resting Mn^{3+}SOD ($\epsilon \approx 850$ M^{-1} cm^{-1} at ~21 000 cm^{-1}) (*22*) and are typical of d → d transitions of six-coordinate Mn^{3+} complexes (*60*), reflecting the more centrosymmetric ligand environment imposed on the Mn^{3+} ion in LT N_3-Mn^{3+}SOD relative to that in the five-coordinate resting state. The LT CD and MCD spectra of N_3-Mn^{3+}SOD provide much more information than the absorption spectrum alone; an iterative Gaussian deconvolution of these three data sets reveals the presence of at least 11 transitions spanning the near-infrared (NIR)/visible/near-UV spectral region (Figure 3 and Table 1). Because bands 1, 2, 6, and 7 are weak in the absorption spectrum but rather intense in the CD and MCD spectra (Figure 3), these bands may be attributed to the four-spin-allowed Mn^{3+} d → d transitions expected for this $3d^4$ ion. The fact that the lowest energy feature (band 1) is observed in the NIR reflects the six-coordinate nature of the Mn^{3+} ion in LT N_3-Mn^{3+}SOD, as noted previously (*5*, *15*). Bands 8−11, which are relatively

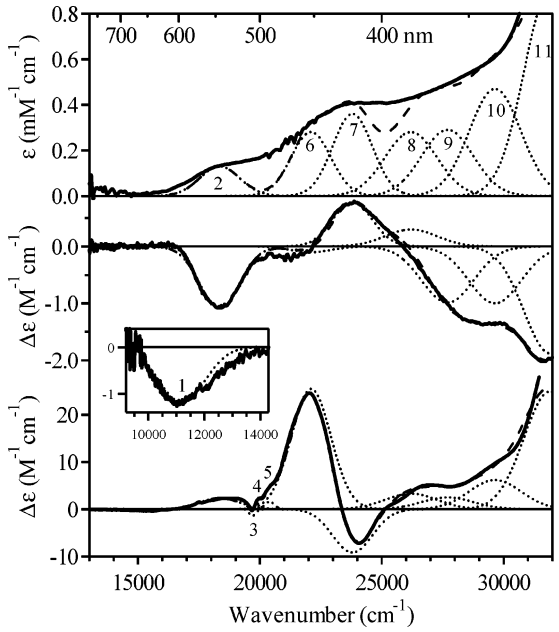

FIGURE 3: electronic absorption (4.5 K) (top), CD (center), and 7 T MCD (bottom) spectra of N_3-Mn^{3+}SOD. (Inset) NIR MCD data (7 T, 4.5 K) of N_3-Mn^{3+}SOD adduct. Individual Gaussian curves (···) and their sums (- - -) obtained from iterative fits of the absorption, CD, and MCD data are displayed on their respective spectra. Conditions, 2.05 mM Mn^{3+}SOD and 183 mM NaN_3 in 50 mM phosphate buffer (pH 7) and 55% (v/v) glycerol.

Table 1: Electronic Transition Energies (cm^{-1}), Oscillator Strengths, f_{exp}, and Bandwidths, $\nu_{1/2}$ (cm^{-1}), Obtained from a Gaussian Analysis of LT Absorption, CD, and MCD Spectra of N_3-Mn^{3+}SOD (see Figure 3)

band	energy	$f_{exp} \times 10^3$	$\nu_{1/2}$	band	energy	$f_{exp} \times 10^3$	$\nu_{1/2}$
1	11 200	ND	1915	7	23 800	3.17	1915
2	18 350	1.14	1915	8	26 600	2.89	2414
3	19 700	ND	333	9	27 800	3.00	2414
4	19 920	ND	233	10	29 550	5.11	2414
5	20 400	ND	458	11	31 900	12.2	2414
6	22 100	2.46	1915				

intense in the absorption spectrum but generally carry minor MCD intensities (Figure 3), are assigned as ligand-to-metal charge transfer (LMCT) transitions. On the basis of a comparison to N_3-Fe^{3+}SOD (*61*) and supported by TD-DFT computations (*vide infra*), the ligand responsible for these LMCT transitions is azide. Bands 3−5, because of their very narrow widths and negligible absorption intensities (Figure 3), are assigned as spin-forbidden (spin-flip) Mn^{3+} d → d transitions. Notably, the absorption and MCD spectra of LT N_3-Mn^{3+}SOD are not altered by a decrease in pH, because spectra collected for LT N_3-Mn^{3+}SOD in pH 5.5 buffer are identical to those in Figure 2 (cf. Figure S2 in the Supporting Information). This result suggests that LT N_3-Mn^{3+}SOD is not a mixture of two differently protonated species, because in that case, the spectroscopic properties of this system would be pH-dependent.

While this analysis provides d → d and LMCT transition energies and intensities for LT N_3-Mn^{3+}SOD (Table 1), it does not afford direct insight into the ground-state properties of this system. Therefore, VTVH MCD spectroscopy, which is a sensitive probe of both ground-state spin Hamiltonian parameters (i.e., *g* values and ZFS parameters) as well as transition polarization, was employed to further characterize this system.

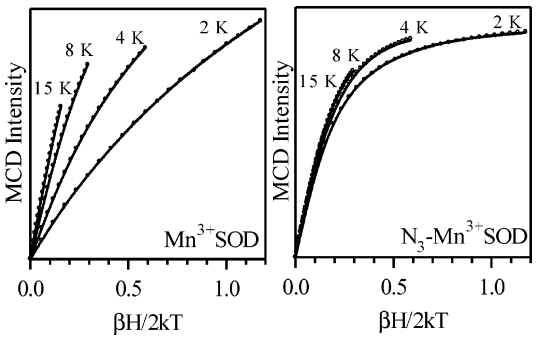

FIGURE 4: (Left) Experimental VTVH MCD data collected at 16 807 cm^{-1} (595 nm) for Mn^{3+}SOD (—) and theoretical fit (○) using the following parameters: $D = 2$ cm^{-1}, $E/D = 0.10$, $g_{iso} = 2.00$, and 21%, *x*; 73%, *y*; and 7%, *z* polarization. (Right) Experimental VTVH MCD data collected at 21 978 cm^{-1} (455 nm) for N_3-Mn^{3+}SOD (—) and theoretical fit (○) using the following parameters: $D = 2.5$ cm^{-1}, $E/D = 0.15$, $g_{iso} = 2.00$, and 30%, *x*; 13%, *y*; and 57%, *z* polarization. See the caption of Figure 2 for sample conditions.

(C) VTVH MCD Data of Mn^{3+}SOD and LT N_3-Mn^{3+}SOD. The addition of N_3^- to Mn^{3+}SOD not only changes the overall appearance of the LT MCD spectrum (Figure 2), but it also significantly alters the VTVH saturation behavior of the MCD signal (Figure 4). Because VTVH MCD data obtained for Mn^{3+}SOD show slow saturation as a function of increasing field and decreasing temperature (left of Figure 4), it was originally suggested that Mn^{3+}SOD has a positive axial ZFS parameter, *D* (*22*). According to LF theory, this sign of *D* would imply a $3d_{z^2}$ orbital ground state, consistent with the trigonal bipyramidal geometry of the Mn^{3+} center in Mn^{3+}SOD (*6*). Importantly, this assignment was corroborated by recent EPR studies of Mn^{3+}SOD, which revealed $D = +2.10$ cm^{-1} (*23*).

VTVH MCD data obtained for LT N_3-Mn^{3+}SOD reveal more rapid saturation of the MCD signal as a function of increasing field and decreasing temperature compared to corresponding data obtained for Mn^{3+}SOD (Figure 4). This saturation behavior of the MCD signal for LT N_3-Mn^{3+}-SOD was assumed to indicate a large effective *g* value for the ground-state doublet, which for this $S = 2$ system would imply that the $M_s = \pm 2$ doublet ($g_{eff} = 8$) is lowest in energy and thus that $D < 0$ cm^{-1} (*22*). Unfortunately, this result could not be verified by EPR spectroscopy, because LT N_3-Mn^{3+}SOD, unlike resting Mn^{3+}SOD, is EPR-silent in parallel mode at X-band frequency (*23*). While the elimination of an EPR signal upon the addition of N_3^- to Mn^{3+}SOD indicates a change in ZFS parameters (*23*), it does not necessarily imply a change in the sign of *D*. Rather, because the EPR signals detected for resting Mn^{3+}SOD are due to transitions within the $M_s = \pm 2$ doublet of the $S = 2$ spin ground state, which is split in zero-field by $3D(E/D)^2$ (*62*), the lack of parallel-mode EPR intensity for LT N_3-Mn^{3+}-SOD may also reflect an increase in the magnitude of *D* and/or the rhombicity (*E/D*) of the system. To quantitatively evaluate the ground-state spin Hamiltonian parameters for this system, we have therefore analyzed the VTVH MCD data for Mn^{3+}SOD and N_3-Mn^{3+}SOD in terms of a recently developed theoretical model (*26*).

Because neither transition polarizations nor ZFS parameters are known for LT N_3-Mn^{3+}SOD, VTVH MCD data for this species were analyzed by systematically varying *D*

and *E/D* from −3 to 3 cm^{-1} and from 0 to 0.3 in increments of 0.5 and 0.05 cm^{-1}, respectively, and for each pair of *D* and *E/D* values, the transition-moment products (i.e., M_{xy}, M_{xz}, and M_{yz}, where the coordinate system corresponds to the principal axes of the **D** tensor) were optimized to fit the experimental data.[3] The goodness of fit was assessed by the χ^2 value, which is the sum of the squares of the differences between the predicted and experimental data. To determine if this fitting procedure of VTVH MCD data yields a unique set (or a range) of ZFS parameters, it was first applied to analyze VTVH MCD data of Mn^{3+}SOD, a system for which both transition polarizations and ZFS parameters have been previously determined (*23*, *28*).

VTVH MCD data obtained for Mn^{3+}SOD at 21 053 and 16 807 cm^{-1} are quite similar (Figure S3 and S4 in the Supporting Information, respectively), consistent with the fact that single-crystal-polarized absorption studies of Mn^{3+}SOD suggest that the d → d transitions responsible for these two MCD features are similarly polarized with respect to the Mn−O(Asp167) bond vector (*28*).[4] Focusing on data collected at 16 807 cm^{-1}, successful fits ($\chi^2 < 0.6$) were obtained with both positive and negative *D* values ($|D| > 1.5$ cm^{-1}) and $E/D = 0-0.33$ (Figure 4 and Figure S4 in the Supporting Information). However, the polarizations necessary to properly fit the VTVH MCD data are drastically different for different signs of *D*. In all cases where $D < -1$ cm^{-1}, the fitting procedure requires a dominant (i.e., ≥90%) *z* polarization, whereas for $D > 0$ cm^{-1}, the transition polarization is slightly more variable (Table S12 in the Supporting Information). Because the polarization of the d → d transition centered at ∼16 807 cm^{-1} has been shown to be tilted ∼40° away from the Mn−O(Asp167) bond vector (on the basis of INDO/S−CI computations (*20*), this bond vector lies in the *xy* plane of the **D** tensor, Figure 1) (*28*), fits of the VTVH MCD data with $D < -1$ cm^{-1} that require ∼90−100% *z* polarization (i.e., essentially perpendicular to this bond vector) can be deemed as unrealistic based on the published single-crystal absorption data. Fits with $D > 1.5$ cm^{-1}, on the other hand, are consistent with experimental data, particularly for $E/D \approx 0.10-0.15$, where good fits ($\chi^2 \leq 0.6$) were achieved with 10−36% *x*, 62−85% *y*, and 0−26% *z* polarization (yielding a transition moment with a major projection onto the Mn−O(Asp167) bond axis). Figure 4 shows simulated VTVH MCD data obtained using ZFS parameters virtually identical to those determined by EPR spectroscopy ($D = 2.11$ cm^{-1}, $E/D = 0.11$) (*23*) and a transition polarization consistent with single-crystal absorption data (*28*). The good agreement between simulated and experimental data demonstrates that our approach to analyze VTVH MCD data of Mn^{3+}SOD yields results consistent with other spectroscopic data and is thus well-suited to obtain a reasonable estimate of the ZFS parameters for LT N_3−Mn^{3+}-SOD from an analysis of corresponding VTVH MCD data.

[3] In these fits, all *g* values were assumed to be 2.00, because deviations of *g* values for Mn^{3+} systems from the free-electron value are generally small. Moreover, minor variations in *g* values (e.g., ∼0.05) did not significantly affect the goodness of fit.

[4] The crystallographic *c* axis, which is the reference vector by which the transition polarizations were determined, is roughly aligned with the Mn−O(Asp167) bond axis, although rotated ∼40° in the equatorial plane toward His171 (*28*), i.e., roughly bisecting the *xy* plane of the **D** tensor (Figure 1).

Table 2: Bond Lengths and Bond Angles for the N_3−Mn^{3+}SOD Active Site as Determined by X-ray Crystallography (PDB file 1MNG-L) and Constrained DFT Energy Minimizations

	1MNG	N_3−$MnSOD^{OH}$	N_3−$MnSOD^{H_2O}$
bond lengths (Å)			
Mn−N(N_2)	2.22	2.38	2.00
Mn−O(sol)	1.95	1.80	2.28
Mn−O(Asp167)	2.25	2.14	2.00
Mn−N(His171)	2.12	2.10	2.18
Mn−N(His26)	2.12	2.12	2.26
Mn−N(His81)	2.07	2.11	2.13
H-bond distances (Å)			
(Osol)H···O(Asp167)		1.67	1.44
(Gln146)H···O(sol)		1.94	1.88
(Gln146)H···O(34)		2.23	2.31
(Tyr34)H···N(N_2)		1.71	1.86
bond angles (deg)			
(His81)N−Mn−N(His171)	148	161	163
(N)N−N−Mn	143	118	123

While VTVH MCD data collected for LT N_3−Mn^{3+}SOD have previously been interpreted as indicating $D < 0$ cm^{-1} (*22*), our analysis does not support this conclusion. In fact, the best fits ($\chi^2 < 0.05$) were actually obtained using $D > 2$ cm^{-1}, $E/D \approx 0.05-0.25$ (Figure S5 in the Supporting Information) and a transition moment oriented predominantly in the *xz* plane, although with a moderate projection on the *y* axis of the **D** tensor (Figure 4 and Table S13 in the Supporting Information; see Figure 1 for **D** tensor orientation). On the basis of these fits as well as INDO/S−CI calculations discussed later, we conclude that LT N_3−Mn^{3+}-SOD actually possesses a positive axial ZFS parameter (i.e., $D > 0$ cm^{-1}) and therefore a $3d_{z^2}$ orbital ground state. Consequently, the strikingly different VTVH MCD saturation behavior exhibited by LT N_3−Mn^{3+}SOD and resting Mn^{3+}-SOD can be accounted for primarily in terms of a change in the transition-moment orientation rather than a change in the sign of *D* and thus the orbital ground state. This result demonstrates that qualitative analysis of VTVH MCD data should be performed cautiously, because many factors contribute to MCD signal saturation behavior.

In summary, our analysis of LT spectroscopic data obtained for N_3−Mn^{3+}SOD has permitted the determination of d → d and LMCT transition energies and provided an estimate of ground-state spin Hamiltonian parameters for this system. These experimental parameters provide an excellent basis for evaluating computational models of LT N_3−Mn^{3+}-SOD, as discussed next.

Computations: (A) LT N_3-Mn^{3+}SOD. Active-site models for six-coordinate, LT N_3−Mn^{3+}SOD were generated by using coordinates from the PDB file (1MNG-L) (*5*) as a starting point for constrained DFT energy minimizations, where the terminal methyl groups of the first-sphere amino acid residues, referred to as the H_3C_β groups, and all atoms of second-sphere residues not involved in the H-bond network were held fixed. Because the protonation state of the coordinated solvent ligand in LT N_3−Mn^{3+}SOD was unclear, models were constructed with both axial OH^- and H_2O ligands, referred to as N_3−$Mn^{3+}SOD^{OH}$ and N_3−Mn^{3+}-SOD^{H_2O}, respectively. The relevant structural parameters of these model systems after geometry optimization as well as structural parameters from X-ray data (*5*) are listed in Table 2. For both models, the Mn−ligand bond lengths of all coordinating amino acid residues are in reasonable agreement

with their crystallographic values, although the two models exhibit a number of notable structural differences. Interestingly, in each case, the N(His81)−Mn−N(His171) angle increased by ∼15−20° during DFT geometry optimization, demonstrating that flexibility in this coordinate is potentially important for allowing small anions to coordinate to the Mn^{3+} center.

In the case of the N_3−$Mn^{3+}SOD^{OH}$ model, the decrease in the Mn−O(sol) distance upon geometry optimization gives rise to a compressed Jahn−Teller axis for this system. Strikingly, the optimized Mn−N(N_2) bond distance is quite long, potentially reflecting the presence of the H bond between azide and the Tyr34 residue in this model (as in the bottom of Figure 1). However, for the geometry-optimized model of N_3−$Mn^{3+}SOD^{H_2O}$, the Mn−N(N_2) and Mn−O(Asp167) bond lengths actually shortened relative to their crystallographically determined values, while the Mn−O(sol) and Mn−N(His26) bond lengths increased quite dramatically (Table 2). Thus, the different Mn−N(N_2) bond lengths observed for our N_3−$Mn^{3+}SOD^{OH}$ and N_3−Mn^{3+}-SOD^{H_2O} models may in fact be attributed to an increase in the anion affinity of the Mn^{3+} center when H_2O is the axial solvent ligand rather than to the H bond between N_3^- and Tyr34, because the latter is present in both models.

It is interesting to note that for our model of N_3−Mn^{3+}-SOD^{H_2O} the additional H^+ (relative to N_3−$Mn^{3+}SOD^{OH}$) remained on the solvent ligand during DFT geometry optimization and did not transfer to the noncoordinating oxygen atom of Asp167. In contrast, computations performed by Li et al. on a N_3−Mn^{3+}SOD model that possessed the same protonation state as our N_3−$Mn^{3+}SOD^{H_2O}$ model indicated that the lowest energy tautomer is the one in which the additional H^+ resides on Asp167 rather than on the axial solvent ligand (*29*). However, the fact that the p*K* value for free aspartic acid is ∼10 pH units lower than that of H_2O (*63*) strongly suggests that the axial solvent ligand is in fact more likely to carry the additional H^+, thus lending credence to the proton distribution observed in our N_3−$Mn^{3+}SOD^{H_2O}$ model.

Because both N_3−$Mn^{3+}SOD^{OH}$ and N_3−$Mn^{3+}SOD^{H_2O}$ are reasonably compatible with X-ray structure data, we sought to estimate the acidity of the coordinated water ligand by calculating the corresponding p*K* value relative to that of Mn^{2+}SOD. Mn^{2+}SOD is generally believed to coordinate H_2O in the axial position at neutral pH (*7*, *8*, *64*), and it has been estimated based on the DFT/electrostatics calculations that the p*K* of this ligand is ∼10−18 (*7*). Using eqs 3−5, the p*K* of the bound water ligand in N_3−Mn^{3+}SOD is determined to be depressed by a $\Delta pK \approx 21$ pH units relative to Mn^{2+}SOD, indicating that H^+ uptake by coordinated solvent upon azide binding to the Mn^{3+} center is extremely unlikely.

To further validate our protonation state assignment for LT N_3−Mn^{3+}SOD, we compared calculated spectroscopic parameters for N_3−$Mn^{3+}SOD^{OH}$ and N_3−$Mn^{3+}SOD^{H_2O}$ with experimental data. For both active-site models, INDO/S−CI calculations predict a rhombic system (for N_3−Mn^{3+}-SOD^{OH}, $D = 1.95$ cm^{-1} and $E/D = 0.193$, and for N_3−$Mn^{3+}SOD^{H_2O}$, $D = 1.49$ cm^{-1} and $E/D = 0.321$). Thus, both sets of calculated ZFS parameters are in reasonable agreement with the results from our analysis of VTVH MCD data collected for LT N_3−Mn^{3+}SOD, which were well-fit

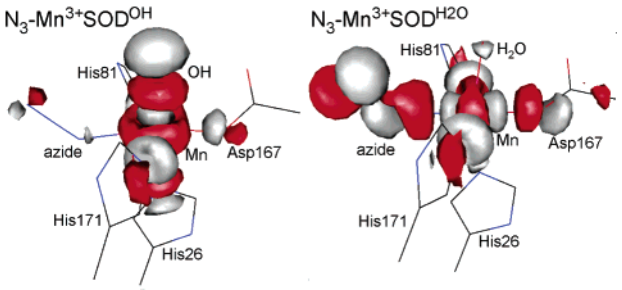

FIGURE 5: Boundary surface plots of the Mn $3d_{z^2}$-based spin-up LUMOs for N_3−$Mn^{3+}SOD^{OH}$ (left) and N_3−$Mn^{3+}SOD^{H_2O}$ (right).

with $D > 2$ cm^{-1} and $E/D \approx 0.05$−0.3 (Table S13 in the Supporting Information). Importantly, the computed ZFS parameters are larger than the corresponding values previously calculated for an active-site model of resting Mn^{3+}-SOD ($D = 1.46$ cm^{-1} and $E/D = 0.019$) (*20*). Because the $M_s = \pm 2$ doublet of a $3d^4$ Mn^{3+} ion is split in zero field by $3D(E/D)^2$ (*62*), the ZFS parameters calculated for N_3−Mn^{3+}-SOD^{OH} and N_3−$Mn^{3+}SOD^{H_2O}$ lead to a predicted splitting of this doublet by 0.22 and 0.46 cm^{-1}, respectively. Thus, the failure to observe a parallel-mode EPR signal at X-band frequency (∼0.3 cm^{-1}) for LT N_3−Mn^{3+}SOD (*23*) may be due to an increase in the magnitude of the ZFS parameters when Mn^{3+}SOD is treated with azide, as predicted for both N_3−$Mn^{3+}SOD^{OH}$ and N_3−$Mn^{3+}SOD^{H_2O}$.

While the calculated ZFS parameters for N_3−$Mn^{3+}SOD^{OH}$ and N_3−$Mn^{3+}SOD^{H_2O}$ are similar, their **D**-tensor orientations are considerably different. For N_3−$Mn^{3+}SOD^{OH}$, the *z* axis of the **D** tensor coincides with the Jahn−Teller compression axis [the O(sol)−Mn−N(His26) vector] and the *y* axis is approximately collinear with the Mn−N(N_2) bond axis. In contrast, the *z* axis of the **D** tensor computed for N_3−Mn^{3+}-SOD^{H_2O} is parallel to the Mn−N(N_2) vector, and the *y* axis lies along the O(sol)−Mn−N(His26) vector. These different **D**-tensor orientations reflect the distinctly different electronic structures of the Mn^{3+} center in these two systems (Figure 5). While in each case the LUMO is predominantly derived from the Mn $3d_{z^2}$ orbital,[5] consistent with $D > 0$ cm^{-1}, for N_3−$Mn^{3+}SOD^{OH}$, the dominant ligand contributions involve the OH^- and His26 groups (left of Figure 5). Alternatively, the LUMO calculated for N_3−$Mn^{3+}SOD^{H_2O}$ displays significant contributions from the N_3^- and Asp167 ligands (right of Figure 5). These differing ligand contributions in the LUMOs have dramatic consequences on the calculated electronic absorption spectra for these two active-site models, as described next.

Figure 6 compares the RT absorption spectrum of LT N_3−Mn^{3+}SOD with simulated absorption spectra for N_3−Mn^{3+}-SOD^{OH} and N_3−$Mn^{3+}SOD^{H_2O}$ based on TD-DFT calculations.[6] The overall appearance of the absorption spectrum predicted for N_3−$Mn^{3+}SOD^{OH}$ agrees quite well with the experimental spectrum obtained for LT N_3−Mn^{3+}SOD.

[5] The large rhombicity computed for N_3−$Mn^{3+}SOD^{H_2O}$ indicates that the $3d_{z^2}$ and $3d_{x^2-y^2}$ orbitals are heavily mixed. Thus, the spin-up LUMO computed for this system, while formally derived from the $3d_{z^2}$ orbital, bears a spatial resemblance to a $3d_{x^2-y^2}$ orbital.

[6] For these simulations, it was assumed that each electronic transition may be described by a Gaussian band with a full width at half-maximum ($\nu_{1/2}$) of 3 000 cm^{-1}, in which case the oscillator strength (f_{calc}) of the electronic transition is related to its molar extinction coefficient ϵ_{max} (M^{-1} cm^{-1}) by $f_{calc} = 4.61 \times 10^{-9} \epsilon_{max} \nu_{1/2}$.

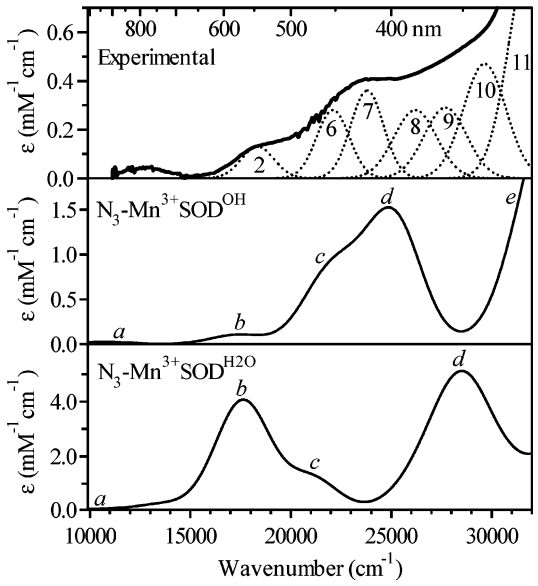

FIGURE 6: (Top) Experimental absorption spectrum of LT $N_3-Mn^{3+}SOD$ (—) and corresponding Gaussian deconvolution (···). (Center and Bottom) Simulated absorption spectra based on TD-DFT computations performed on $N_3-Mn^{3+}SOD^{OH}$ (center) and $N_3-Mn^{3+}SOD^{H_2O}$ (bottom). Note the different scales used for the absorption intensities.

Significantly, the presence of a low-energy Mn^{3+} d → d band at ∼10 700 cm^{-1} (band *a*), which is diagnostic of a six-coordinate Mn^{3+} center (*60*), is consistent with the observation of a NIR feature at ∼11 000 cm^{-1} in the LT MCD spectrum of $N_3-Mn^{3+}SOD$ (inset of Figure 3). Therefore, despite the fact that the optimized $Mn-N(N_2)$ bond length in $N_3-Mn^{3+}SOD^{OH}$ is almost 2.4 Å, the azide ligand still retains a strong interaction with the Mn^{3+} 3d orbitals. In contrast, electronic transition energies and intensities predicted for $N_3-Mn^{3+}SOD^{H_2O}$ are in poor agreement with the experimental data (cf. top and bottom of Figure 6). While a Mn^{3+} d → d transition is again predicted to occur in the NIR (band *a*), an intense ($\epsilon \approx 4\,000$ M^{-1} cm^{-1}) N_3^- → Mn^{3+} CT transition is predicted at ∼17 500 cm^{-1} (band *b*) that has no counterpart in the experimental spectrum. The appearance of this prominent feature for $N_3-Mn^{3+}SOD^{H_2O}$ can be understood by noting that an intense N_3^- → Mn^{3+} CT transition will occur in the visible spectral region whenever the unoccupied Mn 3d-based MO lies along the $(N_2)N-Mn-O(Asp167)$ axis (*20*). This prediction is based upon the facts that (i) for a N_3^- → Mn^{3+} CT transition to be intense, the Mn^{3+} 3d-based acceptor MO must contain significant contributions from N_3^--based orbitals (as in the right of Figure 5) and (ii) only N_3^- → Mn^{3+} CT transitions for which the sole unoccupied Mn^{3+} 3d-based MO is the acceptor orbital will occur in the visible spectral region, because excitation into any of the singly occupied Mn^{3+} 3d-based MOs formally generates an excited $S = {}^3/_2$ Mn^{2+} ion, thus shifting the CT transition into the near UV. When the TD-DFT-computed absorption spectra for $N_3-Mn^{3+}SOD^{OH}$ and $N_3-Mn^{3+}SOD^{H_2O}$ along with the results from our ΔpK calculation (*vide supra*) are taken together, they provide strong evidence that azide binding to Mn^{3+}-SOD is not accompanied by H^+ uptake and suggest that our $N_3-Mn^{3+}SOD^{OH}$ model provides a reasonable description of the LT $N_3-Mn^{3+}SOD$ active site.

Having validated the $N_3-Mn^{3+}SOD^{OH}$ model on the basis of spectroscopic and computational data, it is now warranted to use TD-DFT computations performed on this model as a basis for developing detailed spectral assignments for LT $N_3-Mn^{3+}SOD$. Hence, band 1 of LT $N_3-Mn^{3+}SOD$ (inset of Figure 3), which occurs in the NIR spectral region, is assigned as the Mn $3d_{x^2-y^2} \rightarrow 3d_{z^2}$ transition, consistent with an earlier qualitative spectral analysis within the framework of ligand-field theory (*15*). TD-DFT computations for $N_3-Mn^{3+}SOD^{OH}$ also corroborate our tentative assignment of bands 2, 6, and 7 as d → d transitions. Specifically, our computations indicate that the feature at ∼18 000 cm^{-1} (band *b*), corresponding to band 2 in the experimental spectrum of LT $N_3-Mn^{3+}SOD$ (Figure 6), originates from the Mn $3d_{xz} \rightarrow 3d_{z^2}$ transition. Bands 6 and 7 are attributed to the Mn $3d_{xy} \rightarrow 3d_{z^2}$ and Mn $3d_{yz} \rightarrow 3d_{z^2}$ transitions, respectively. Because the N_3^- π nonbonding orbitals are properly oriented for strong overlap with the Mn $3d_{xy}$- and $3d_{yz}$-based MOs, bands 6 and 7 are predicted to carry a significant amount of N_3^- → Mn^{3+} CT character, leading to the high intensities of these formally forbidden d → d transitions. Notably, the large admixture of N_3^- → Mn^{3+} CT character into these transitions has been experimentally verified by resonance Raman studies of $N_3-Mn^{3+}SOD$ (*20*).

TD-DFT computations performed on $N_3-Mn^{3+}SOD^{OH}$ also reveal that multiple N_3^- → Mn^{3+} CT transitions, which are mixed with His → Mn^{3+} and Asp167 → Mn^{3+} CT transitions, contribute to bands *d* and *e* (center of Figure 6). Specifically, N_3^- → Mn^{3+} CT transitions terminating in the Mn^{3+} t_{2g}- and e_g-derived MOs (using symmetry labels of the parent O_h point group) give rise to bands *d* and *e*, respectively, where transitions contributing to the former band are predicted to be roughly half as intense as those giving rise to the latter band. Thus, on the basis of their moderate intensities in the absorption spectrum, bands 8 and 9 of LT $N_3-Mn^{3+}SOD$ can be assigned as N_3^- → Mn^{3+} t_{2g}-type CT transitions, while the more intense bands 10 and 11 are attributed to N_3^- → Mn^{3+} e_g-type CT transitions. On the basis of the N_3^- → Mn^{3+} CT character of bands *d* and *e*, the energies of these bands are expected to be sensitive to the N_3-Mn^{3+} bond distance. In fact, a decrease in the N_3-Mn distance of ∼0.10 Å is sufficient to blue-shift band *d* by ∼4 000 cm^{-1} (i.e., to ∼29 000 cm^{-1}), resulting in better agreement between computed and experimental LMCT transition energies, perhaps suggesting that the N_3-Mn^{3+} distance of our $N_3-Mn^{3+}SOD^{OH}$ model is a slight overestimate of the true N_3-Mn^{3+} distance.

(B) Hypothetical Active-Site Models of the Product-Inhibited Form of MnSOD. Because of the success of our computational methods in the study of LT $N_3-Mn^{3+}SOD$, we used a similar approach to generate and evaluate hypothetical active-site models of the dead-end complex that is formed when MnSOD is treated with $O_2^{\cdot-}$ (*12*) or H_2O_2 (*13*). Bull et al. proposed that the dead-end complex results from oxidative addition of $O_2^{\cdot-}$ to $Mn^{2+}SOD$ and specifically suggested the formation of a side-on peroxo-Mn^{3+} adduct (*12*). Because the oxidative addition of superoxide to Mn^{2+}-SOD may lead to several active-site structures, we generated models to evaluate the following viable scenarios: (i) proton transfer from coordinated H_2O to bulk solvent upon oxidation of Mn^{2+}, yielding a seven-coordinate side-on peroxo-Mn^{3+} adduct, (η^2-O_2)$-Mn^{3+}SOD^{OH}$; (ii) dissociation of coordinated

Table 3: Bond Lengths, Bond Angles, and Relative Energies of the Peroxo-Mn^{3+}SOD Active-Site Models

	($\eta^{2-}O_2$)−$Mn^{3+}SOD^{OH}$	($\eta^{2-}O_2$)−$Mn^{3+}SOD^{H_2O}$	H30V ($\eta^{2-}O_2$)−$Mn^{3+}SOD^{H_2O}$
bond lengths (Å)			
Mn−O1	1.88	1.80	1.80
Mn−O2	1.93	2.22	2.26
1O−O2	1.44	1.40	1.40
Mn−O(sol)	1.91	2.40	2.44
Mn−O(Asp167)	2.51	2.16	2.07
Mn−N(His26)	2.74	2.28	2.23
Mn−N(His171)	2.17	2.20	2.22
Mn−N(His81)	2.14	2.13	2.15
H-bond distances (Å)			
O(sol)H···O(Asp167)	1.83	1.48	1.52
(Gln146)H···O(sol)	1.60	1.87	1.88
(Gln146)H···O(Tyr34)	2.26	2.27	2.10
bond angles (deg)			
N(His81)−Mn−N(His171)	165	166	162
O1−Mn−O2	44	40	38
O2−O1−Mn	66	54	53
relative energy (kcal/mol)[a]	NA[b]	1.38	NA

[a] Energy at convergence relative to that of our HOO−$Mn^{3+}SOD^{OH}$[Tyr34] model. [b] Not applicable (see the text).

Table 4: Bond Lengths, Bond Angles, and Relative Energies of the Hydroperoxo-Mn^{3+}SOD Active-Site Models

	HOO−$Mn^{3+}SOD^{OH}$[Tyr34]	HOO−$Mn^{3+}SOD^{OH}$	O(H)O−$Mn^{3+}SOD^{OH}$	H30V HOO−$Mn^{3+}SOD^{OH}$
bond lengths (Å)				
Mn−O1	2.19	1.99	2.70	1.87
1O−O2	1.51	1.49	1.50	1.47
O1−H	NA[a]	NA	0.98	NA
O2−H	0.98	0.98	NA	0.98
Mn−O(sol)	1.81	1.84	1.80	1.86
Mn−O(Asp167)	2.27	2.08	2.06	1.95
Mn−N(His26)	2.19	2.15	2.18	2.30
Mn−N(His171)	2.08	2.17	2.07	2.29
Mn−N(His81)	2.06	2.17	2.11	2.26
H-bond distances (Å)				
O(sol)H···O(Asp167)	1.66	1.81	1.62	1.78
(Gln146)H···O(sol)	1.88	1.84	1.97	1.92
(Gln146)H···O(Tyr34)	2.32	2.24	2.24	2.09
(Tyr34)H···O2	2.13	NA	1.59	NA
bond angles (deg)				
N(His81)−Mn−N(His171)	162	160	145	170
O2−O1−Mn	127	115	NA	114
relative energy (kcal/mol)[b]	0	4.72	7.75	NA

[a] Not applicable (see the text). [b] Energy at convergence relative to that of our HOO−$Mn^{3+}SOD^{OH}$[Tyr34] model.

H_2O to yield a six-coordinate side-on peroxo-Mn^{3+} adduct, (η^2-O_2)−$Mn^{3+}SOD^{H_2O}$; (iii) proton transfer from coordinated H_2O to the terminal O atom of the nascent peroxo ligand, O2, yielding a hydroperoxo-Mn^{3+} adduct, HOO−Mn^{3+}-SOD^{OH}; and (iv) proton transfer from coordinated H_2O to the proximal O atom of the nascent peroxo ligand, O1, also yielding a hydroperoxo-Mn^{3+} adduct but with the coordinated O atom protonated, O(H)O−$Mn^{3+}SOD^{OH}$. The initial coordinates of these models were based on the X-ray structure of N_3−Mn^{3+}SOD (PDB file 1MNG-L), and the azide ligand was replaced with either a side-on-bound O_2^{2-} ligand [initially oriented such that the Mn−O(Asp167) bond axis bisected the O1−O2 vector] or an end-on-bound HOO^- ligand. To assess whether the existence of a H bond between Tyr34 and O2 could aid in the formation of a hydroperoxo-Mn^{3+} adduct, two models of HOO−Mn^{3+}SOD were generated, one with the phenolic H^+ of Tyr34 oriented toward O2 and one with this H^+ oriented away from the HOO^- ligand (referred to as HOO−$Mn^{3+}SOD^{OH}$[Tyr34] and HOO−$Mn^{3+}SOD^{OH}$, respectively).[7] All of these hypothetical models of the dead-end complex were subjected to constrained DFT energy minimizations where the H_3C_β groups of the first-sphere residues and all atoms of second-sphere residues not involved in the H-bond network were held fixed. Relevant structural parameters for these models after DFT geometry optimization as well as the relative energies of (η^2-O_2)−$Mn^{3+}SOD^{H_2O}$, HOO−Mn^{3+}SOD[Tyr34], HOO−$Mn^{3+}SOD^{OH}$, and O(H)O−$Mn^{3+}SOD^{OH}$, all of which possess identical charges as well as the same number and type of atoms, are given in Tables 3 and 4.

(η^2-O_2)−$Mn^{3+}SOD^{OH}$. Our geometry optimized (η^2-O_2)−$Mn^{3+}SOD^{OH}$ model exhibits very large Mn−O(Asp167) and Mn−N(His26) distances of >2.5 Å, whereas all other Mn^{3+}−ligand distances are comparable to those of other computationally derived Mn^{3+}SOD models (Table 3) (*20*, *28*, *29*). These anomalously long Mn−O(Asp167) and Mn−N(His26) distances are due to movement of the Mn^{3+} ion toward the

[7] The possibility of a H bond between Tyr34 and the O2 atom of a side-on-bound O_2^{2-} ligand (i.e., in our (η^2-O_2)−$Mn^{3+}SOD^{OH}$ and (η^2-O_2)−$Mn^{3+}SOD^{H_2O}$ models) was also evaluated. In these cases, models with and without the H bond had virtually identical geometries and TD-DFT-computed absorption spectra, although models in which this H bond was present were ∼2 kcal/mol lower in energy than the corresponding models lacking the (Tyr34)OH···O2 H bond.

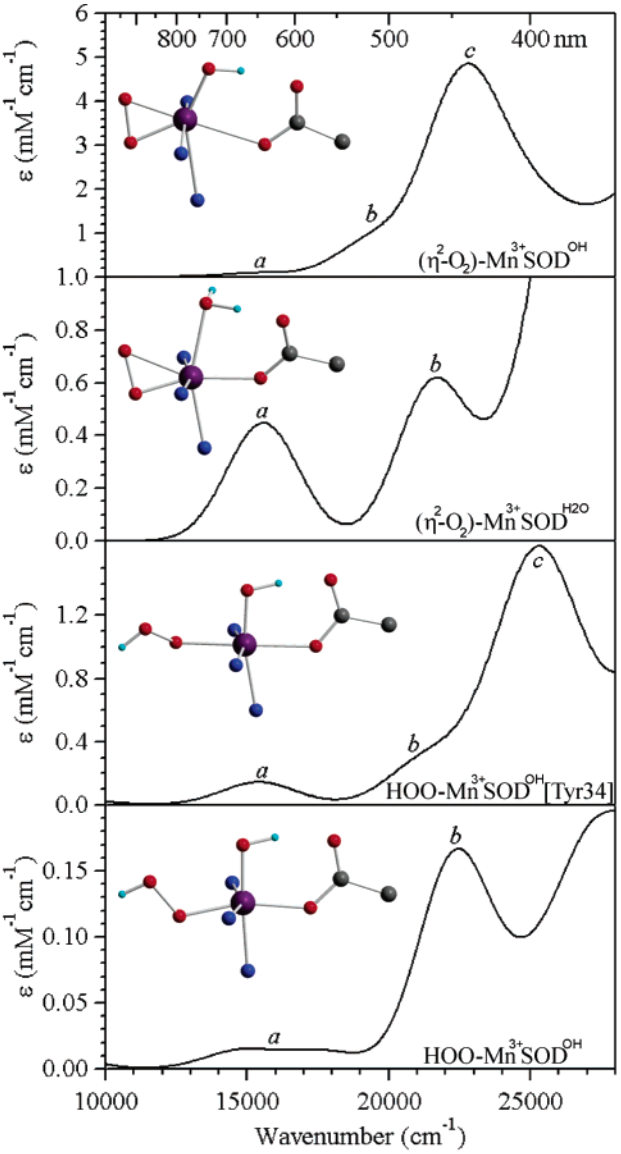

FIGURE 7: Simulated absorption spectra based on TD-DFT computations performed on $(\eta^2\text{-}O_2)-Mn^{3+}SOD^{OH}$, $(\eta^2\text{-}O_2)-Mn^{3+}SOD^{H_2O}$, $HOO-Mn^{3+}SOD^{OH}$[Tyr34], and $HOO-Mn^{3+}SOD^{OH}$. Truncated versions of the active-site models used for the TD-DFT computations are shown as insets next to their corresponding spectra. Note for comparison that the product-inhibited form of MnSOD exhibits absorption features at ~15 400 and 24 400 cm^{-1} ($\epsilon \approx 0.23$ and 0.70 mM^{-1} cm^{-1}, respectively) (*12*, *13*).

substrate (analogue) binding pocket, thereby lessening the steric bulk created by the side-on O_2-Mn^{3+} core [note that the N(His81)−Mn−N(His171) angle increased by ~15° during geometry optimization]. Concomitantly, the OH^- ligand, initially located trans to N(His26), moved toward Asp167 (Figure 7), also aiding the active site to adopt the side-on O_2-Mn^{3+} geometry.

To determine if the spectroscopic properties of $(\eta^2\text{-}O_2)-Mn^{3+}SOD^{OH}$ are consistent with those of the dead-end complex, the absorption spectrum of this hypothetical active-site model was computed using the TD-DFT method. The computed spectrum (Figure 7) exhibits a moderately intense ($\epsilon \approx 1000$ M^{-1} cm^{-1}) d → d band at ~19 300 cm^{-1} (band *b*) and a rather intense ($\epsilon \approx 5000$ M^{-1} cm^{-1}) $O_2^{2-} \rightarrow Mn^{3+}$ CT transition at ~22 500 cm^{-1} (band *c*). Because the presence of these intense features in the visible spectral region is in obvious disagreement with the absorption spectrum reported for the dead-end complex, which only exhibits two modestly intense features ($\epsilon \approx 230$ and 700 M^{-1} cm^{-1}) at ~15 400 and 24 400 cm^{-1} (*12*, *13*), $(\eta^2\text{-}O_2)-Mn^{3+}SOD^{OH}$ is a poor model of the dead-end complex.

$(\eta^2\text{-}O_2)-Mn^{3+}SOD^{H_2O}$. Geometry optimization of $(\eta^2\text{-}O_2)-Mn^{3+}SOD^{H_2O}$ yielded a seven-coordinate Mn^{3+} center, albeit with rather long Mn−O(sol), Mn−N(His26), and Mn−O2 bond lengths in the range of ~2.2−2.4 Å (Table 3). While seven-coordinate Mn^{3+} complexes are rare, precedent for this coordination number does exist (*65*). A notable structural feature of the $(\eta^2\text{-}O_2)-Mn^{3+}SOD^{H_2O}$ model is that the H_2O ligand remained coordinated during the geometry optimization, as it had been proposed that dissociation of this ligand constitutes a prerequisite for the formation of a side-on-bound peroxo complex (*13*). The optimized structure of $(\eta^2\text{-}O_2)-Mn^{3+}SOD^{H_2O}$ does, however, reveal that the O(sol) and O2 atoms appear to "repel" one another, as evidenced by the long Mn−O2 bond length and the shift of the H_2O ligand toward Asp167 (Table 3 and Figure 7). Consequently, the O_2-Mn^{3+} core of this model is quite asymmetric, almost intermediate between the side-on and end-on peroxo descriptions.

The TD-DFT-computed absorption spectrum of $(\eta^2\text{-}O_2)-Mn^{3+}SOD^{H_2O}$ shown in Figure 7 exhibits two rather prominent d → d bands in the visible region at ~15 500 and 21 500 cm^{-1} ($\epsilon \approx 450$ and 700 M^{-1} cm^{-1}, respectively). Importantly, the energies and intensities of these d → d transitions are reasonably consistent with the absorption features reported for the dead-end complex (*12*, *13*). While the intensity ratio of the higher and lower energy transitions in the computed absorption spectrum of ~1.5 is smaller than the experimental ratio of ~3, estimated from the published absorption spectrum of the dead-end complex (*12*), this discrepancy is well within the expected accuracy of the TD-DFT method. Consequently, the geometric and electronic structures of the $(\eta^2\text{-}O_2)-Mn^{3+}SOD^{H_2O}$ model appear to mimic those of the dead-end complex reasonably well.

$HOO-Mn^{3+}SOD^{OH}$[Tyr34] and $HOO-Mn^{3+}SOD^{OH}$. The optimized geometries of the $HOO-Mn^{3+}SOD^{OH}$[Tyr34] and $HOO-Mn^{3+}SOD^{OH}$ models are quite similar, both qualitatively resembling our $N_3-Mn^{3+}SOD^{OH}$ model (Table 4). The presence of a H bond between Tyr34 and O2 in the $HOO-Mn^{3+}SOD^{OH}$[Tyr34] model, however, has a significant influence on the optimized Mn−O1 and Mn−O(Asp167) bond lengths (Table 4), causing both to increase when this H bond is present. Such an increase in the $O1-Mn^{3+}$ bond length is indeed expected, because the H bond from Tyr34 to O2 stabilizes the hydroperoxo orbitals, thus rendering HOO^- a weaker donor to the Mn^{3+} ion. Because of their structural similarities to $N_3-Mn^{3+}SOD^{OH}$, it is not surprising that the TD-DFT-computed absorption spectra of $HOO-Mn^{3+}SOD^{OH}$[Tyr34] and $HOO-Mn^{3+}SOD^{OH}$ are in good agreement with the experimental spectrum of the dead-end complex (Figure 7). Specifically, computed spectra for both models exhibit a weak feature at ~15 000 cm^{-1} ($\epsilon \approx 150$ and 15 M^{-1} cm^{-1}, respectively) and a more intense band at ~22 200−25 000 cm^{-1} ($\epsilon \approx 1600$ and 160 M^{-1} cm^{-1}, respectively). Moreover, the character of many of the electronic transitions computed for these models are virtually identical. For example, TD-DFT computations for both $HOO-Mn^{3+}SOD^{OH}$[Tyr34] and $HOO-Mn^{3+}SOD^{OH}$ predict

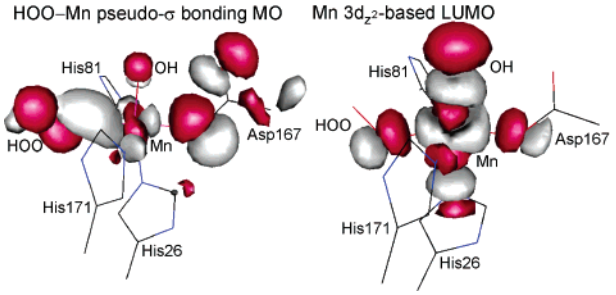

FIGURE 8: Boundary surface plots of the spin-up HOO−Mn^{3+} pseudo-σ-bonding MO (left) and the Mn $3d_{z^2}$-based spin-up LUMO (right) for HOO−$Mn^{3+}SOD^{OH}$[Tyr34].

a Mn^{3+} d → d transition and a weak HOO^- → Mn^{3+} CT transition to give rise to the absorption feature at ∼15 000 cm^{-1} (band *a*).

However, closer examination of the TD-DFT results reveals a number of important electronic differences between HOO−$Mn^{3+}SOD^{OH}$[Tyr34] and HOO−$Mn^{3+}SOD^{OH}$, all of which can be understood in terms of the differences in Mn−O1 and Mn−O(Asp167) bond lengths in these two models. Most significantly, band *c* of HOO−$Mn^{3+}SOD^{OH}$[Tyr34] is an order of magnitude more intense than band *b* of HOO−$Mn^{3+}SOD^{OH}$ (Figure 7), a difference that can be rationalized by the nature of the electronic transitions contributing to these bands. For HOO−$Mn^{3+}SOD^{OH}$[Tyr34], a HOO^- → Mn^{3+} CT transition, where the donor MO is the hydroperoxo-based HOO^-−Mn^{3+} pseudo-σ-bonding MO and the acceptor MO is the Mn^{3+} 3d-based LUMO (Figure 8), gives rise to band *c* at ∼25 000 cm^{-1}. The moderately large absorption intensity of this feature is due to the large amount of HOO^- and O(Asp167) ligand character in both the donor and acceptor MOs (Figure 8). A corresponding HOO^- → Mn^{3+} CT transition of similar intensity is also predicted for HOO−$Mn^{3+}SOD^{OH}$, albeit at a much higher energy (∼33 000 cm^{-1}). The blue shift of this CT transition can be explained by the shorter Mn−O1 bond length present for HOO−$Mn^{3+}SOD^{OH}$ (Table 4), which leads to a greater stabilization of the donor MO relative to the acceptor MO (Figure 8). Because of the lack of intense CT features, the visible region of the computed absorption spectrum of HOO−Mn^{3+}SOD is dominated by a d → d transition (band *b*) of low intensity (Figure 7).

While the computed absorption spectra for our HOO−$Mn^{3+}SOD^{OH}$[Tyr34] and HOO−$Mn^{3+}SOD^{OH}$ models are quite different, both are in sufficiently close agreement with that reported for the dead-end complex (*12*) that neither model may be deemed inconsistent based on this alone. However, the DFT-computed total energies of these optimized models (Table 4) reveal that a H bond between Tyr34 and the HOO^- ligand stabilizes the HOO−Mn^{3+} motif by an additional ∼5 kcal/mol, thus favoring our HOO−Mn^{3+}-SOD^{OH}[Tyr34] model. Importantly, with this H bond present, the HOO−$Mn^{3+}SOD^{OH}$[Tyr34] model is slightly lower in energy than its (η^2-O_2)−$Mn^{3+}SOD^{H_2O}$ isomer (cf. Tables 3 and 4).

O(H)O−$Mn^{3+}SOD^{OH}$. While DFT geometry optimizations of all other hypothetical active-site models of the dead-end complex yielded peroxo- or hydroperoxo-Mn^{3+} adducts, geometry optimization of O(H)O−$Mn^{3+}SOD^{OH}$ led to dissociation of the hydroperoxo group, resulting in an active-site model with an O1···Mn distance of ∼2.7 Å and an O2···HO(Tyr34) distance of 1.6 Å (Table 4). This optimized geometry is strikingly similar to the geometry that we have recently proposed for the five-coordinate, RT form of N_3−Mn^{3+}SOD (*20*), where the active-site Mn^{3+} ion resembles that of resting Mn^{3+}SOD and the anion forms a strong H bond with the phenolic H^+ of Tyr34. The DFT-computed energy of our geometry-optimized O(H)O−Mn^{3+}SOD model is ∼8 kcal/mol higher than that calculated for HOO−Mn^{3+}-SOD[Tyr34], which is not surprising given the drastically different geometries of these two models (Table 4). However, on the basis of the relative p*K* values, H^+ transfer from Tyr34 [experimental p*K* ≈ 9.5 (*66*)] to HOO^- to form H_2O_2 (p*K* ≈ 11.6) is expected to be thermodynamically favorable and therefore may help drive HOO^- dissociation. The fact that the phenolic proton of Tyr34 did not transfer to the HOO^- group during the geometry optimization of O(H)O−Mn^{3+}-SOD may be understood by noting that, (i) except for the phenolic H^+, Tyr34 atom positions were fixed in our geometry optimization, thus precluding structural changes accompanying Tyr34 deprotonation, and (ii) X-ray data of Mn^{3+}SOD reveal an outer-sphere H_2O molecule H-bonded to Tyr34 and His30 (top of Figure 1) that was not included in our initial model of O(H)O−$Mn^{3+}SOD^{OH}$. The addition of this crystallographically detected H_2O molecule to our O(H)O−$Mn^{3+}SOD^{OH}$ model followed by subsequent DFT geometry optimization resulted in the isolation of both a local and global minimum differing in energy by ∼9.6 kcal/mol. The structure associated with the local minimum resembled that of our O(H)O−Mn^{3+}SOD model without the second-sphere H_2O molecule, with the O1 atom ∼ 2.7 Å from the Mn^{3+} ion and the O2 atom ∼ 1.5 Å from the phenolic H^+ of Tyr34. In contrast, the structure associated with the global minimum (Figure 9) features a deprotonated Tyr34 residue and a H_2O_2 molecule.

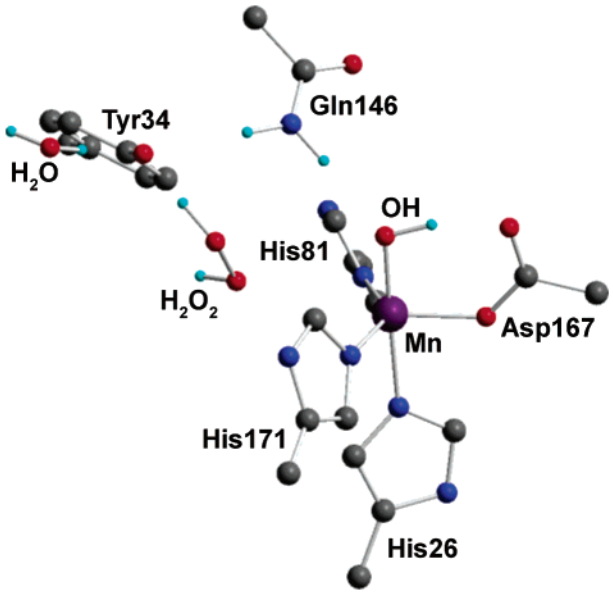

FIGURE 9: Active-site model of O(H)O−$Mn^{3+}SOD^{OH}$ with an outer-sphere H_2O molecule near Tyr34, obtained from a constrained DFT geometry optimization. Note that the H^+ bound to the phenolic O atom of Tyr34 in the resting state has transferred to the HOO^- molecule to generate H_2O_2 and a tyrosinate anion.

DISCUSSION

Although LT N_3-Mn^{3+}SOD has been the subject of previous spectroscopic (*15*, *22*) and computational (*29*) studies, important questions concerning the electronic properties of this species and their implications with respect to the dead-end complex had yet to be explored. Originally, it was proposed that dissimilarities in MCD and VTVH MCD data of Mn^{3+}SOD in the absence and presence of azide reflect a change in the orbital ground state of the Mn^{3+} center and, consequently, that the active-site geometry changes from trigonal bipyramidal to square pyramidal (*22*). However, it has been known for almost 10 years that azide binding to Mn^{3+}SOD actually yields a pseudo-octahedral, six-coordinate N_3-Mn^{3+} adduct at LT (*5*, *15*, *18*). Our analysis of LT absorption, CD, MCD, and VTVH MCD data of N_3-Mn^{3+}-SOD within the framework of DFT, INDO/S−CI, and TD-DFT computations provides evidence that N_3^- binding to the Mn^{3+} center causes neither a change in orbital ground state nor H^+ uptake by the coordinated solvent, both of which had been previously proposed (*22*, *29*). Application of our computational methods to evaluate hypothetical models of the product-inhibited form of MnSOD suggests that, on the basis of their relative energies and TD-DFT-computed absorption spectra, both a side-on peroxo- and an end-on hydroperoxo-Mn^{3+} adduct are reasonable descriptions of the dead-end complex. Below, published kinetic data are used as a means to further discriminate between these two species, and possible implications of our results with respect to the catalytic cycle of MnSOD are explored.

Nature of the Dead-End Complex. In our $HOO-Mn^{3+}$-SOD^{OH}[Tyr34] model, the H bond between Tyr34 and HOO^- both lowers the total energy of this model (Table 4) and appreciably effects the TD-DFT-computed absorption spectrum (Figure 7). Thus, if $HOO-Mn^{3+}SOD^{OH}$[Tyr34] effectively mimicked the geometric and electronic features of the dead-end complex, then replacement of Tyr34 would disfavor formation of this species and alter its absorption spectrum. However, Silverman and co-workers observed neither of these effects in their study of a MnSOD variant in which Tyr34 was mutated to Phe (*13*, *67*). In fact, Y34F MnSOD actually displayed increased susceptibility to product inhibition (*13*), contrary to what would be expected if a H bond from Tyr34 assisted in the formation of this species. A subsequent study showed that the kinetics describing the formation and decay of the dead-end complex are indeed only slightly altered by the Y34F mutation (*67*), providing further evidence against Tyr34 playing a role in stabilizing the dead-end complex. Additionally, the absorption spectra reported for the dead-end complexes of WT and Y34F MnSODs are virtually identical, although extinction coefficients were not determined for the mutant species (*13*). Collectively, these results strongly suggest that $HOO-Mn^{3+}$-SOD^{OH}[Tyr34] may be discounted as a model of the dead-end complex.

There are also several lines of evidence that argue against the dead-end complex as being an end-on hydroperoxo-Mn^{3+} adduct lacking a H bond from Tyr34. First, our $HOO-Mn^{3+}$-SOD^{OH} model is ~4 kcal/mol higher in energy than the (η^2-O_2)$-Mn^{3+}SOD^{H_2O}$ model possessing a side-on O_2-Mn^{3+} adduct, indicating that, in the absence of a H bond between Tyr34 and O2, a side-on-bound peroxo ligand is more stable than an end-on-bound hydroperoxo ligand. Second, studies of human MnSOD revealed that mutation of Gln143 (analogous to Gln146 of *E. coli* MnSOD) to a variety of other amino acid residues such as Asn and Ala, none of which is capable of donating a strong H bond to coordinated solvent, does not appear to prevent the formation of the dead-end complex (*68*, *69*).[8] If deprotonation of the axial solvent ligand were required to form the dead-end complex, then abolishing a H bond to the coordinated solvent by these Q143X mutations would affect this deprotonation event. Indeed, DFT/electrostatics computations performed by Noodleman and co-workers estimated that the Q143N mutation increases the acidity of coordinated H_2O in Mn^{2+}SOD by ~4−8 pH units relative to WT Mn^{2+}SOD (*7*). Third, the absorption spectra of the dead-end complexes of WT and H30V MnSODs [where in the latter case the outer-sphere His30 residue (Figure 1) has been mutated to Val] are very similar (*27*), suggesting that this mutation does not greatly alter the geometric and electronic properties of the dead-end complex. As born out by X-ray structure data, the H30V mutation places one of the methyl carbon atoms of the Val30 residue (specifically, the Cγ2 atom) 4.5 Å from the manganese ion (*27*), a reduction of 1.5 Å relative to the distance between the Nδ1 atom of His30 and the metal ion observed for native MnSOD (*6*). Further evidence of this tightening of the substrate (analogue) binding pocket is provided by the fact that azide does not interact with the active-site Mn^{3+} ion of the mutant protein at RT (*27*).

To investigate if the presence of Val30 would possibly prevent the formation of hydroperoxo-Mn^{3+} or peroxo-Mn^{3+} adducts, an active-site model of the H30V MnSOD mutant was constructed based on the PDB file 1N0N, an end-on-bound hydroperoxo ligand or a side-on-bound peroxo ligand were added [generating H30V $HOO-Mn^{3+}SOD^{OH}$ and H30V (η^2-O_2)$-Mn^{3+}SOD^{H_2O}$, respectively], and a constrained DFT geometry optimization was performed, in which the H_3C_β groups of the first-sphere residues and all atoms of second-sphere residues not involved in the H-bond network were held fixed. Our geometry optimized model of H30V $HOO-Mn^{3+}SOD^{OH}$ shows that the presence of Val30 leads to a decrease in the O1−Mn bond length by ~0.1 Å and an increase in all (His)N−Mn bond lengths by ~0.1−0.2 Å (Table 4). Importantly, the TD-DFT-computed absorption spectra of WT and H30V $HOO-Mn^{3+}SOD^{OH}$ are substantially different (top of Figure 10), indicating that the structural changes in the $HOO-Mn^{3+}$ core caused by the H30V substitution would notably alter the absorption spectrum of the dead-end complex provided that this structural motif was present; however, this is not observed experimentally (*27*). Alternatively, the optimized structures of the WT and H30V (η^2-O_2)$-Mn^{3+}SOD^{H_2O}$ models are very similar (Table 3), and consequently, their TD-DFT-computed absorption spectra are also quite similar (bottom of Figure 10). When taken together, only our (η^2-O_2)$-Mn^{3+}SOD^{H_2O}$ model appears consistent with all of the available spectroscopic and kinetic data reported for the dead-end complex, although further experimental examination of the geometric and

[8] While it was reported that formation of the dead-end complex for the Q143X mutants (where X stands for A or N) is much slower than for the WT enzyme, this difference is likely due to an increase in the $Mn^{3+/2+}$ reduction potential accompanying the Q143X mutations (*7*, *69*).

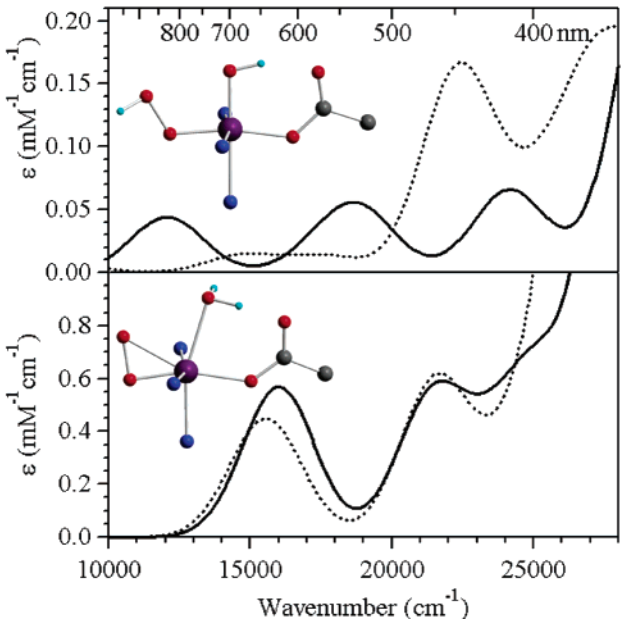

FIGURE 10: Simulated absorption spectra based on TD-DFT computations performed on H30V HOO−$Mn^{3+}SOD^{OH}$ (top) and H30V (η^2-O_2)−$Mn^{3+}SOD^{H_2O}$ (bottom). Truncated versions of the active-site models used for the TD-DFT computations are shown as insets next to their corresponding spectra. For comparison, the TD-DFT-computed absorption spectra of HOO−$Mn^{3+}SOD^{OH}$ (top, ···) and (η^2-O_2)−$Mn^{3+}SOD^{H_2O}$ (bottom, ···) are reproduced from Figure 7. Note for comparison that the product-inhibited form of MnSOD exhibits absorption features at ∼15 400 and 24 400 cm^{-1} ($\epsilon \approx 0.23$ and 0.70 mM^{-1} cm^{-1}, respectively) (*12*, *13*).

electronic properties of this species are necessary to corroborate this proposal.

LT N_3-Mn^{3+}SOD and Its Implications for $O_2^{\cdot-}$ Oxidation by Mn^{3+}SOD. Until about 5 years ago, quantitative analyses of VTVH MCD data for $S > {}^1/_2$ systems of low symmetry were generally not possible. However, recent advances in MCD theory (*26*, *70*) now permit interpretation of VTVH MCD data obtained for any spin system in terms of the ground-state spin Hamiltonian parameters and transition polarizations (*71*). Application of this methodology to LT N_3−Mn^{3+}SOD reveals that our VTVH MCD data are consistent with both positive and negative values of *D* (Figure S5 and Table S13 in the Supporting Information). While it was previously proposed that *D* is negative because of the rapid saturation of the MCD signal as a function of the magnetic field (*22*), INDO/S−CI computations on our active-site model of LT N_3−$Mn^{3+}SOD^{OH}$ actually predict a positive *D* value ($D = 1.95$ cm^{-1}). These computations also reveal that the binding of N_3^- to Mn^{3+}SOD results in an increase in *D* and *E/D* values, providing a rationale for the EPR silence of N_3−Mn^{3+}SOD in parallel-mode experiments at X-band frequency (*23*). Therefore, we conclude that binding of N_3^- to Mn^{3+}SOD does not result in a change in sign of *D* and that both resting Mn^{3+}SOD and six-coordinate N_3−Mn^{3+}SOD actually possess a Mn^{3+} $3d_{z^2}$ ground state where the *z* axis is collinear with the O(sol)−Mn−N(His26) axis (left of Figure 5). This finding is important because it has been proposed that azide binding to the active-site Mn^{3+} ion reorients the redox active (unoccupied) Mn 3d-based MO (*22*) such that this MO develops a pseudo-σ bond with N_3^-. Instead, our DFT results for the N_3−$Mn^{3+}SOD^{OH}$ model indicate that this N_3^-−Mn^{3+} pseudo-σ-bonding interaction actually involves the singly occupied Mn $3d_{x^2-y^2}$-based MO. In the case of N_3−$Mn^{3+}SOD^{H_2O}$, however, the Mn 3d-based LUMO is indeed a N_3^-−Mn^{3+} pseudo-σ-bonding MO (right of Figure 5), indicating that, when substrate (analogue) binding is coupled with protonation of the axial solvent ligand, the redox-active MO may reorient.

On the basis of qualitative considerations, it has been suggested that charge donation from azide to the Mn^{3+} center is sufficient to cause protonation of the axial solvent ligand (*29*). In light of the electronic similarities that exist between N_3^- and substrate $O_2^{\cdot-}$, it was subsequently proposed that oxidation of $O_2^{\cdot-}$ by Mn^{3+}SOD (eq 2a) proceeds by (i) coordination of $O_2^{\cdot-}$ to the Mn^{3+} center, (ii) proton transfer from Gln146 to the axial OH^- ligand, which is favored by charge donation from superoxide to the Mn^{3+} ion, and (iii) reduction of the Mn^{3+} center by superoxide, although it was noted that the H^+ and electron transfers to $O_2^{\cdot-}$ could be concerted (*7*). Our DFT calculations, however, reveal that N_3−Mn^{3+}SOD is considerably more acidic than Mn^{2+}SOD ($\Delta pK \approx -21$). and furthermore, the TD-DFT-computed absorption spectrum of N_3−$Mn^{3+}SOD^{OH}$ but not N_3−Mn^{3+}-SOD^{H_2O} is consistent with the experimental absorption spectrum of LT N_3−Mn^{3+}SOD (Figure 6). Collectively, these results indicate that N_3^- binding to Mn^{3+}SOD does not result in proton transfer to the axial OH^- ligand. Insofar as N_3^- is a suitable electronic mimic of substrate superoxide, it therefore appears reasonable to conclude that $O_2^{\cdot-}$ binding to the active-site Mn^{3+} ion alone is insufficient to cause protonation of the axial solvent ligand. While it has been suggested that the presence of an anionic OH^- ligand would prevent electron transfer from $O_2^{\cdot-}$ to Mn^{3+}SOD (*7*), precedent for $O_2^{\cdot-}$ reduction of a Mn^{3+} ion coordinated by anionic ligands is provided by Mn^{3+}(EDTA) (ethylenediaminetetraacetic acid) and related Mn^{3+} complexes, which are rapidly reduced by $O_2^{\cdot-}$ (*72*). Nevertheless, the reduction of Mn^{3+}SOD to Mn^{2+}SOD without protonation of coordinated OH^- is expected to be quite unfavorable; i.e., Noodleman and co-workers have used DFT/electrostatics computations to show that the $Mn^{3+}SOD^{OH}$ → $Mn^{2+}SOD^{OH}$ reduction potential is ∼0.5 V lower than the corresponding $Mn^{3+}SOD^{OH}$ → $Mn^{2+}SOD^{H_2O}$ reduction potential (*7*). Thus, while our results suggest that a stepwise mechanism involving protonation of coordinated solvent followed by electron transfer from $O_2^{\cdot-}$ to the Mn^{3+} ion is unlikely, redox considerations clearly indicate that these processes must be intimately coupled and may very well proceed by a concerted mechanism.

Mechanism of Reduction of $O_2^{\cdot-}$ by Mn^{2+}SOD. It has long been assumed that proton uptake by coordinated solvent upon Mn^{3+}SOD reduction (eq 2a) provides a mechanism for H^+ storage by MnSOD that may facilitate $O_2^{\cdot-}$ reduction to H_2O_2 in the other half-reaction (eq 2b) (*8*, *73*). Because the reduction of superoxide in the absence of $O_2^{\cdot-}$ protonation is quite unfavorable, Mn^{2+}SOD could overcome this energetic barrier by coupling $O_2^{\cdot-}$ reduction to proton transfer from the coordinated solvent (*74*). Our DFT geometry optimization of O(H)O−Mn^{3+}SOD indeed shows that protonation at the proximal O atom of nascent peroxide leads to HOO^- dissociation and the generation of an active-site structure resembling that of resting Mn^{3+}SOD (Table 4). Importantly, Tyr34 is properly oriented to develop a H-bonding interaction with dissociated HOO^-, and when a H_2O

molecule occupies the cavity formed by Tyr34 and His30, Tyr34 donates its phenolic H^+ to HOO^- to generate H_2O_2 (Figure 9). Thus, our DFT results provide computational support for the notion that Tyr34 provides one of the two protons required in the generation of H_2O_2, which had been previously inferred by noting that the active-site p*K* of Mn^{3+}-SOD is due to Tyr34 deprotonation at high pH (p*K* ≈ 9.5) (*21*, *30*, *66*). According to this model, H^+ transfer from Tyr34 to HOO^- is facilitated by H-bond donation to the phenolic group from an outer-sphere water molecule. In light of a report that this H_2O molecule is involved in an extensive H-bond network that also includes His30 and Tyr174 (*5*), it is not surprising that mutations of His30 and Tyr174 decrease catalytic activity (*75*, *76*) and effectively abolish the active-site p*K* (*77*) associated with Tyr34 deprotonation (*30*, *66*). In fact, any disruption of this H-bonding chain involving Tyr174, His30, exogenous H_2O, Tyr34, Gln146, and the coordinated solvent would prevent rapid H^+ delivery to $O_2^{\cdot-}$. Indeed, the work of Silverman and co-workers has shown that disruption of this proton relay by outer-sphere mutations generally increases the susceptibility of MnSOD to product inhibition by slowing the catalytic reduction of $O_2^{\cdot-}$ rather than directly favoring the formation of the dead-end complex (*13*, *27*, *67*−*69*, *75*, *76*). Because the formation of the dead-end complex competes with the catalytic reduction of the substrate (Scheme 1), any drop in the efficiency of this step will tend to increase product inhibition. Thus, MnSOD requires a delicately tuned H-bond network involving an ensemble of second- and third-sphere residues along with properly positioned solvent molecules to achieve maximum catalytic efficiency.

ACKNOWLEDGMENT

We thank Dr. Frank Neese (MPI Mülheim, Germany) for providing a free copy of ORCA and for useful discussions.

SUPPORTING INFORMATION AVAILABLE

VTVH MCD data for LT N_3−Mn^{3+}SOD at 16 807 cm^{-1} and Mn^{3+}SOD at 21 053 cm^{-1} (Figures S1 and S3), 4.5 K absorption and 7 T MCD spectra of LT N_3−Mn^{3+}SOD in pH 5.5 buffer (Figure S2), ZFS parameters, transition polarizations, and χ^2 values determined by fitting VTVH MCD data for Mn^{3+}SOD and LT N_3−Mn^{3+}SOD (Figures S4 and S5 and Tables S12 and S13), and all Cartesian coordinates for all DFT energy-minimized active-site models (Tables S1−S11). This material is available free of charge via the Internet at http://pubs.acs.org.

REFERENCES

1. Miller, A.-F., and Sorkin, D. L. (1997) Superoxide dismutases: A molecular perspective, *Comments Mol. Cell. Biophys. 9*, 1−48.
2. Packer, L. (2002) in *Methods in Enzymology* (Abelson, J. N., and Simon, M. I., Eds.) pp 400, Academic Press, San Diego, CA.
3. Miller, A.-F. (2004) in *Comprehensive Coordination Chemistry II* (McCleverty, J. A., and Meyer, T. J., Eds.) pp 479−506, Elsevier Ltd., Oxford, U.K.
4. Ludwig, M. L., Metzger, A. L., Pattridge, K. A., and Stallings, W. C. (1991) Manganese superoxide-dismutase from *Thermus thermophilus*. A structural model refined at 1.8 Å resolution, *J. Mol. Biol. 219*, 335−358.
5. Lah, M. S., Dixon, M. M., Pattridge, K. A., Stallings, W. C., Fee, J. A., and Ludwig, M. L. (1995) Structure−function in *Escherichia coli* iron superoxide dismutase: Comparisons with the manganese enzyme from *Thermus thermophilus*, *Biochemistry 34*, 1646−1660.
6. Edwards, R. A., Baker, H. M., Whittaker, M. M., Whittaker, J. W., Jameson, G. B., and Baker, E. N. (1998) Crystal structure of *Escherichia coli* manganese superoxide dismutase at 2.1 Å resolution, *J. Biol. Inorg. Chem. 3*, 161−171.
7. Han, W.-G., Lovell, T., and Noodleman, L. (2002) Coupled redox potentials in manganese and iron superoxide dismutases from reaction kinetics and density functional/electrostatics calculations, *Inorg. Chem. 41*, 205−218.
8. Miller, A.-F., Padmakumar, F., Sorkin, D., Karapetian, A., and Vance, C. K. (2003) Proton-coupled electron transfer in Fe-superoxide dismutase and Mn-superoxide dismutase, *J. Inorg. Biochem. 93*, 71−83.
9. Pick, M., Rabani, J., Yost, F., and Fridovich, I. (1974) The catalytic mechanism of the manganese-containing superoxide dismutase of *Escherichia coli* studied by pulse radiolysis, *J. Am. Chem. Soc. 96*, 7329−7333.
10. McAdam, M. E., Fox, R. A., Lavelle, F., and Fielden, E. M. (1977) A pulse-radiolysis study of the manganese-containing superoxide dismutase from *Bacillus stearothermophilus*. A kinetic model for the enzyme action, *Biochem. J. 165*, 71−79.
11. McAdam, M. E., Lavelle, F., Fox, R. A., and Fielden, E. M. (1977) A pulse-radiolysis study of the manganese-containing superoxide dismutase from *Bacillus stearothermophilus*. Further studies on the properties of the enzyme, *Biochem. J. 165*, 81−87.
12. Bull, C., Niederhoffer, E. C., Yoshida, T., and Fee, J. A. (1991) Kinetic studies of superoxide dismutases: Properties of the manganese-containing protein from *Thermus thermophilus*, *J. Am. Chem. Soc. 113*, 4069−4076.
13. Hearn, A. S., Tu, C. K., Nick, H. S., and Silverman, D. N. (1999) Characterization of the product inhibited complex in catalysis by human manganese superoxide dismutase, *J. Biol. Chem. 274*, 24457−24460.
14. Davis, C. A., Hearn, A. S., Fletcher, B., Bickford, J., Garcia, J. E., Lévêque, V., Melendez, J. A., Silverman, D. N., Zucali, J., Agarwal, A., and Nick, H. S. (2004) Potent anti-tumor effects of an active site mutant of human manganese-superoxide dismutase, *J. Biol. Chem. 279*, 12769−12776.
15. Whittaker, M. M., and Whittaker, J. W. (1996) Low-temperature thermochromism marks a change in coordination for the metal ion in manganese superoxide dismutase, *Biochemistry 35*, 6762−6770.
16. Kitajima, N., Komatsuzaki, H., Hikichi, S., Osawa, M., and Moro-oka, Y. (1994) A monomeric side-on peroxo manganese(III) complex: $Mn(O_2)$(3,5-iPr_2pzH)(HB(3,5-iPr_2pz)$_3$), *J. Am. Chem. Soc. 116*, 11596−11597.
17. Neese, F., and Solomon, E. I. (1998) Detailed spectroscopic and theoretical studies on $[Fe(EDTA)(O_2)]^{3-}$: Electronic structure of the side-on ferric-peroxide bond and its relevance to reactivity, *J. Am. Chem. Soc. 120*, 12829−12848.
18. Whittaker, M. M., and Whittaker, J. W. (1997) A "thermophilic shift" in ligand interactions for *Thermus thermophilus* manganese superoxide dismutase, *J. Biol. Inorg. Chem. 2*, 667−671.
19. Whittaker, J. W. (1997) A model for local melting of metalloprotein structure, *J. Phys. Chem. B 101*, 674−677.
20. Jackson, T. A., Karapetian, A., Miller, A.-F., and Brunold, T. C. (2004) Spectroscopic and computational studies of the azide-adduct of manganese superoxide dismutase: Definitive assignment of the ligand responsible for the low-temperature thermochromism, *J. Am. Chem. Soc. 126*, 12477−12491.
21. Hsu, J. L., Hsieh, Y. S., Tu, C. K., O'Connor, D., Nick, H. S., and Silverman, D. N. (1996) Catalytic properties of human manganese superoxide dismutase, *J. Biol. Chem. 271*, 17687−17691.
22. Whittaker, J. W., and Whittaker, M. M. (1991) Active site spectral studies on manganese superoxide dismutase, *J. Am. Chem. Soc. 113*, 5528−5540.
23. Campbell, K. A., Yikilmaz, E., Grant, C. V., Gregor, W., Miller, A.-F., and Britt, R. D. (1999) Parallel polarization EPR characterization of the Mn^{III} center of oxidized manganese superoxide dismutase, *J. Am. Chem. Soc. 121*, 4714−4715.
24. Vance, C. K., and Miller, A.-F. (1998) Spectroscopic comparisons of the pH dependencies of Fe-substituted (Mn)superoxide dismutase and Fe-superoxide dismutase, *Biochemistry 37*, 5518−5527.

25. Vance, C. K., and Miller, A.-F. (1998) A simple proposal that can explain the inactivity of metal-substituted superoxide dismutases, *J. Am. Chem. Soc. 120*, 461−467.
26. Neese, F., and Solomon, E. I. (1999) MCD C-term signs, saturation behavior, and determination of band polarizations in randomly oriented systems with spin $S \geq {}^1/_2$. Application to $S = {}^1/_2$ and $S = {}^5/_2$, *Inorg. Chem. 38*, 1847−1865.
27. Hearn, A. S., Stroupe, M. E., Cabelli, D. E., Ramilo, C. A., Luba, J. P., Tainer, J. A., Nick, H. S., and Silverman, D. N. (2003) Catalytic and structural effects of amino acid substitution at histidine 30 in human manganese superoxide dismutase: Insertion of valine Cγ into the substrate access channel, *Biochemistry 42*, 2781−2789.
28. Whittaker, M. M., Ekberg, C. A., Edwards, R. A., Baker, E. N., Jameson, G. B., and Whittaker, J. W. (1998) Single-crystal polarized spectroscopy of manganese superoxide dismutase and electronic structure of the active site metal complex, *J. Phys. Chem. B 102*, 4668−4677.
29. Li, J., Fisher, C. L., Konecny, R., Lovell, T., Bashford, D., and Noodleman, L. (1999) Density functional and electrostatic calculations of manganese superoxide dismutase active site complexes in protein environments, *Inorg. Chem. 38*, 929−939.
30. Jackson, T. A., Xie, J., Yikilmaz, E., Miller, A.-F., and Brunold, T. C. (2002) Spectroscopic and computational studies on iron and manganese superoxide dismutases: Nature of the chemical events associated with active site p*K*s, *J. Am. Chem. Soc. 124*, 10833−10845.
31. Carrasco, R., Morgenstern-Badarau, I., and Cano, J. (2003) Charge transfers influence on the spin ground state of manganese and iron superoxide dismutases: A DFT study on a model of the reduced active site interacting with O_2^-, *Chem. Commun.* 436−437.
32. te Velde, G., Bickelhaupt, F. M., van Gisbergen, S. J. A., Guerra, C. F., Baerends, E. J., Snijders, J. G., and Ziegler, T. (2001) Chemsitry with ADF, *J. Comput. Chem. 22*, 931−967.
33. Guerra, C. F., Snijders, J. G., te Velde, G., and Baerends, E. J. (1998) Towards an order-n DFT method, *Theor. Chem. Acc. 99*, 391−403.
34. *ADF2003.01*, SCM, Theoretical Chemistry, Vrije Universiteit, Amsterdam, The Netherlands, http://www.scm.com.
35. Vosko, S. H., Wilk, L., and Nusair, M. (1980) Accurate spin-dependent electron liquid correlation energies for local spin density calculations: A critical analysis, *Can. J. Phys. 58*, 1200−1211.
36. Becke, A. D. (1986) Density functional calculations of molecular bond energies, *J. Chem. Phys. 84*, 4524−4529.
37. Perdew, J. P. (1986) Density functional approximation for the correlation energy of the inhomogeneous electron gas, *Phys. Rev. B 33*, 8822−8824.
38. Neese, F. (2002) *Orca−An ab initio, density functional, and semiempirical program package*, Version 2.2, Max Planck Institut für Strahlenchemie, Mülheim, Germany.
39. Ridley, J., and Zerner, M. C. (1973) An intermediate neglect of differential overlap technique for spectroscopy: Pyrrole and the azines, *Theor. Chim. Acta 32*, 111−134.
40. Zerner, M. C., Loew, G. H., Kirchner, R. F., and Mueller-Westerhof, U. T. (1980) An intermediate neglect of differential overlap technique for spectra of transition-metal complexes: Ferrocene, *J. Am. Chem. Soc. 102*, 589−599.
41. Bacon, A. D., and Zerner, M. C. (1979) An intermediate neglect of differential overlap theory for transition-metal complexes, *Theor. Chim. Acta 53*, 21−54.
42. Becke, A. D. (1993) A new mixing of Hartree−Fock and local-density-functional theories, *J. Chem. Phys. 98*, 1372−1377.
43. Becke, A. D. (1993) Density-functional thermochemistry. III. The role of exact exchange, *J. Chem. Phys. 98*, 5648−5652.
44. Lee, C., Yang, W., and Parr, R. G. (1988) Development of the Colle−Salvetti correlation-energy formula into a functional of the electron density, *Phys. Rev. B 37*, 785−789.
45. Schäfer, A., Horn, H., and Ahlrichs, R. (1992) Fully optimized contracted Gaussian basis sets for atoms lithium to krypton, *J. Chem. Phys. 97*, 2571−2577.
46. The Ahlrichs auxiliary basis sets were obtained from the turbomole basis set library under ftp.chemie.uni-karlsruhe.de/pub/cbasen. Weigend, F.; Häser, M. (1997) *97*, 331−340.
47. Schäfer, G., Huber, C., and Ahlrichs, R. (1994) Fully optimized contracted Gaussian basis sets of triple-ζ valence quality for atoms Li to Kr, *J. Chem. Phys. 100*, 5829−5835.
48. Laaksonen, L. (1992) A graphics program for the analysis and display of molecular dynamics trajectories, *J. Mol. Graphics 10*, 33−34.
49. Bergman, D. L., Laaksonen, L., and Laaksonen, A. (1997) Visualization of solvation structures in liquid mixtures, *J. Mol. Graphics Modell. 15*, 301−306.
50. Bauernschmitt, R., and Ahlrichs, R. (1996) Treatment of electronic excitations within the adiabatic approximation of time dependent density functional theory, *Chem. Phys. Lett. 256*, 454−464.
51. Casida, E. M., Jamorski, C., Casida, K. C., and Salahub, D. R. (1998) Molecular excitation energies to high-lying bound states from time-dependent density-functional response theory: Characterization and correction of the time-dependent local density approximation ionization threshold, *J. Chem. Phys. 108*, 4439−4449.
52. Stratman, R. E., Scuseria, G. E., and Frisch, M. J. (1998) An efficient implementation of time-dependent density-functional theory for the calculation of excitation energies of large molecules, *J. Chem. Phys. 109*, 8218−8224.
53. Hirata, S., and Head-Gordon, M. (1999) Time-dependent density functional theory for radicals: An improved description of excited states with substantial double excitation character, *Chem. Phys. Lett. 302*, 375−382.
54. Hirata, S., and Head-Gordon, M. (1999) Time-dependent density functional theory within the Tamm−Dancoff approximation, *Chem. Phys. Lett. 314*, 291−299.
55. Neese, F., and Olbrich, G. (2002) Efficient use of the resolution of the identity approximation in time-dependent density functional calculations with hybrid density functionals, *Chem. Phys. Lett. 362*, 170−178.
56. Jackson, T. A., Yikilmaz, E., Miller, A.-F., and Brunold, T. C. (2003) Spectroscopic and computational study of a non-heme iron $\{Fe-NO\}^7$ system: Exploring the geometric and electronic structures of the nitrosyl adduct of iron superoxide dismutase, *J. Am. Chem. Soc. 125*, 8348−8363.
57. Konecny, R., Li, J., Fisher, C. L., Dillet, V., Bashford, D., and Noodleman, L. (1999) CuZn superoxide dismutase geometry optimization, energetics, and redox potential calculations by density functional and electrostatic methods, *Inorg. Chem. 38*, 940−950.
58. Li, J., Fisher, C. L., Chen, J. L., Bashford, D., and Noodleman, L. (1996) Calculation of redox potentials and pK_a values of hydrated transition metal cations by a combined density functional and continuum dielectric theory, *Inorg. Chem. 35*, 4694−4702.
59. Noodleman, L., Lovell, T., Han, W.-G., Li, J., and Himo, F. (2004) Quantum chemical sudies of intermediates and reaction pathways in selected enzymes and catalytic synthetic systems, *Chem. Rev. 104*, 459−508.
60. Lever, A. B. P. (1984) *Inorganic Electronic Spectroscopy*, 2nd ed., Elsevier, Amsterdam, The Netherlands.
61. Xie, J., Yikilmaz, E., Miller, A.-F., and Brunold, T. (2002) Second-sphere contributions to substrate−analog binding in iron(III) superoxide dismutase, *J. Am. Chem. Soc. 124*, 3769−3774.
62. Krzystek, J., Yeagle, G. J., Park, J.-H., Britt, R. D., Meisel, M. W., Brunel, L.-C., and Telser, J. (2003) High-frequency and -field EPR spectroscopy of tris(2,4-pentanedionato)manganese(III): Investigation of solid-state versus solution Jahn−Teller effects, *Inorg. Chem. 42*, 4610−4618.
63. Voet, D., Voet, J. G., and Pratt, C. W. (1998) *Fundamentals of Biochemistry*, John Wiley and Sons, Inc., New York.
64. Stallings, W. C., Metzger, A. L., Pattridge, K. A., Fee, J. A., and Ludwig, M. L. (1991) Structure−function relationships in iron and manganese superoxide dismutases, *Free Radical Res. Commun. 12−13*, 259−268.
65. Dabrowiak, J. C., Nafie, L. A., Bryan, P. S., and Torkelson, A. T. (1977) Accessibility of manganese oxidation states. Control of pentaaza macrocyclic ligands, *Inorg. Chem. 16*, 540−544.
66. Maliekal, J., Karapetian, A., Vance, C., Yikilmaz, E., Wu, Q., Jackson, T., Brunold, T. C., Spiro, T. G., and Miller, A.-F. (2002) Comparison and contrasts between the active site p*K*s of Mn-superoxide dismutase and those of Fe-superoxide dismutase, *J. Am. Chem. Soc. 124*, 15064−15075.
67. Guan, Y., Hickey, M. J., Borgstahl, G. E. O., Hallewell, R. A., Lepock, J. R., O'Connor, D., Hsieh, Y. S., Nick, H. S., Silverman, D. N., and Tainer, J. A. (1998) Crystal structure of Y34F mutant human mitochondrial manganese superoxide dismutase and the functional role of tyrosine 34, *Biochemistry 37*, 4722−4730.
68. Hsieh, Y. S., Guan, Y., Tu, C. K., Bratt, P. J., Angerhofer, A., Lepock, J. R., Hickey, M. J., Tainer, J. A., Nick, H. S., and

Silverman, D. N. (1998) Probing the active site of human manganese superoxide dismutase: The role of glutamine 143, *Biochemistry 37*, 4731−4739.
69. Lévêque, V. J.-P., Stroupe, M. E., Lepock, J. R., Cabelli, D. E., Tainer, J. A., Nick, H. S., and Silverman, D. N. (2000) Multiple replacements of glutamine 143 in human manganese superoxide dismutase: Effects on structure, stability, and catalysis, *Biochemistry 39*, 7131−7137.
70. Oganesyan, V. S., George, S. J., Cheesman, M. R., and Thomson, A. J. (1999) A novel, general method of analyzing magnetic circular dichroism spectra and magnetization curves of high-spin metal ions: Application to the protein oxidized rubredoxin, *Desulfovibrio gigas*, *J. Chem. Phys. 110*, 762−777.
71. Kirk, M. L., and Peariso, K. (2003) Recent applications of MCD spectroscopy to metalloenzymes, *Curr. Opin. Chem. Biol. 7*, 220−227.
72. Stein, J., Fackler, J. P. J., McClune, G. J., Fee, J. A., and Chan, L. T. (1979) Superoxide and manganese(III). Reactions of Mn−EDTA and Mn−CyDTA complexes with O_2^-. X-ray structure of KMnEDTA·2H_2O, *Inorg. Chem. 18*, 3511−3519.
73. Whittaker, M. M., and Whittaker, J. W. (1997) Mutagenesis of a proton linkage pathway in *Escherichia coli* manganese superoxide dismutase, *Biochemistry 36*, 8923−8931.
74. Miller, A.-F. (2004) Superoxide dismutases: Active sites that save, but a protein that kills, *Curr. Opin. Chem. Biol. 8*, 162−168.
75. Hearn, A. S., Fan, L., Lepock, J. R., Luba, J. P., Greenleaf, W. B., Cabelli, D. E., Tainer, J. A., Nick, H. S., and Silverman, D. N. (2004) Amino acid substitution at the dimeric interface of human manganese superoxide dismutase, *J. Biol. Chem. 279*, 5861−5866.
76. Ramilo, C. A., Lévêque, V., Guan, Y., Lepock, J. R., Tainer, J. A., Nick, H. S., and Silverman, D. N. (1999) Interrupting the hydrogen bond network at the active site of human manganese superoxide dismutase, *J. Biol. Chem. 274*, 27711−27716.
77. Edwards, R. A., Whittaker, M. M., Whittaker, J. W., Baker, E. N., and Jameson, G. B. (2001) Removing a hydrogen bond in the dimer interface of *Escherichia coli* manganese superoxide dismutase alters structure and reactivity, *Biochemistry 40*, 4622−4632.

BI048639T